Estimation of Rainfall Rates in Tropical Cyclones
by Passive Microwave Radiometry

A REPORT

from the space science and engineering center
the university of wisconsin-madison
madison, wisconsin

Estimation of Rainfall Rates in Tropical Cyclones
by Passive Microwave Radiometry

A Summary Report to the

National Oceanic and Atmospheric Administration

Grant #NA78-SAC-04320

For the Period of

30 September 1978 to 30 September 1982

Submitted by

James A. Weinman

Space Science and Engineering Center
at the University of Wisconsin-Madison
1225 West Dayton Street
Madison, WI 53706

January 1983

Overview:

The report of Olson et al. enclosed in this report summarizes attempts to derive rainfall rates from noisy simulated microwave data such as might be expected from the Scanning Multifrequency Microwave Radiometer, SMMR, on SEASAT. It is demonstrated in this report that data with 4°k random noise, a pessimistic estimate, can still provide rainfall estimates that are good to 30%. While this result looks promising, the extraction of such rainfall information requires the analysis of data from eight channels simultaneously. The radiometer footprint size varies with frequency so that the radiometers may be measuring radiation from differing amounts of rain. The brief report by Chin et al. presents results of a technique designed to restore the spatial resolution of all of the data to a common optimal size so that it can then be processed in accord with Olson's algorithm.

The work described above was conducted before actual SMMR data was available; this situation was remedied during the summer of 1982. We were surprised to find 37GHz brightness temperatures as low as 165° associated with heavy midlatitude precipitation. This observation led to the appreciation that ice hydrometeors may be required in radiative transfer models. (Wilheit et al. (1982) also recently incorporated ice hydrometeors in his analysis of 19GHz aircraft measurements of precipitations). Olson, along with most of the modeling community, disregarded the effect of ice hydrometeors. It should however be noted that Beer (1980) found no evidence of ice hydrometeors in his analysis of the 37GHz images of Cyclone Joan. The importance of ice hydrometeors in tropical cyclones requires more study so that the inference

from Olson's research should be regarded as preliminary. This study is being recast to incorporate the radiative effects of ice particles.

REFERENCES

Beer, T., 1980. Satellite Microwave Estimation of Tropical Cyclone Rainfall: A Case Study of Cyclone Joan. Australian Meteorological Magazine 28, 155-166.

Wilheit, T.T., A.T.C. Chang, J.L. King, E.B. Rodgers, R.A. Neiman, B.M Krupp, A.S. Milman, J.R. Stratigos, H. Siddalingaiah, 1982. Microwave Radiometric Observations Near 19.35, 92, and 183GHz of Precipitation in Tropical Storm Cora. J. App. Met. 21, 1137-1145.

5/SCRATCH/02

ESTIMATION OF RAINFALL RATES IN TROPICAL CYCLONES
BY PASSIVE MICROWAVE RADIOMETRY

W. S. OLSON[1]*

J. A. WEINMAN[1,2]

H. M. WOOLF[2,3]

(1) Dept. of Meteorology, University of Wisconsin, Madison, Wisconsin

(2) Space Science and Engineering Center, University of Wisconsin, Madison, Wisconsin

(3) National Oceanic and Atmospheric Administration, National Earth Satellite Service

ABSTRACT

A numerical model has been developed to study the transfer of microwave radiation (6.63 to 37 GHz) through a plane-parallel cloud of hydrometeors. The effects of multiple-scattering within the cloud, as well as polarization by the underlying sea surface are considered in this formulation. Model parameters characteristic of tropical cyclone rain cells over the ocean are specified, and the resulting microwave intensities emerging from cloud top are calculated.

A sensitivity study indicates that the upwelling cloud-top intensity is responsive to changes in the precipitation column height and surface reflectivity over the range of frequencies and rainfall rates considered. Variations in sea surface reflectivity may be induced by wind stress or roughening by raindrop impaction.

Regression equations derived from model-generated, synthetic brightness temperature data at the Scanning Multichannel Microwave Radiometer frequencies form the basis of a rainfall rate inversion method presented in this study. It is demonstrated that rainfall rate estimates within an error bound of 30% might be achieved at rainfall rates greater than 4 mm/hr, despite significant levels of noise in the data. The applicability of this method is contingent upon improvements in SMMR image resolution that would allow the delineation of individual tropical cyclone raincells.

1. Introduction

Methods for inferring the intensity and distribution of rainfall have been a focus of research efforts in tropical cyclone meteorology. Since a net latent heating of the atmosphere occurs in the process of drop formation, precipitation measurements can yield important information on storm energetics.

The utilization of satellite-borne microwave radiometers to make rainfall observations was initiated with the launching of the Electrically Scanning Microwave Radiometer (ESMR) instruments on Nimbus 5 and 6. Microwave brightness temperature (intensity) measurements by the Nimbus 5 ESMR, with a center frequency of 19.35 GHz, were used by Allison, et al. (1974) to map rainfall areas in Hurricane Ava and other tropical disturbances.

An analysis of the radiative transfer problem by Wilheit, et al. (1977) demonstrated that the upwelling brightness temperature at 19.35 GHz was sensitive to both rainfall rate and the height of the precipitation column. Subsequently Rodgers and Adler (1979) derived a semi-empirical relationship between Nimbus 5 ESMR brightness temperatures and rainfall rates which accounted for the variability of the precipitation column height. This relationship was applied with some success to several tropical cyclonic storms to determine trends in the magnitude and distribution of precipitation and latent heating.

Weinman and Guetter (1977) developed a method for delineating areas of rainfall over land and water surfaces on the basis of Nimbus 6 ESMR (37 GHz) brightness temperature measurements. Such model computations were later employed by Beer (1980) to estimate rainfall rates in Cyclone Joan. The ESMR-derived rainfall distributions in Cyclone Joan were in qualitative agreement with radar returns.

The potential for mapping regions of tropical cyclone rainfall has been demonstrated by the ESMR studies. However, the accuracy of rainfall rate estimates from single-frequency passive microwave radiometry has, so far, been less than satisfactory for most applications, Austin and Geotis (1978). Upwelling microwave brightness temperatures at the ESMR frequencies are not functions of rainfall rate alone. Changes in other environmental parameters, such as precipitation column height, Wilheit, et al. (1977), and surface emissivity/reflectivity, Webster, et al. (1976), can also significantly affect the upwelling microwave radiances. Roughly speaking, the number of independent sensor channels should be equal to or greater than the number of unknown geophysical parameters in the system. Unfortunately only one microwave channel (19.35 GHz, one polarization) was available on Nimbus 5 and two channels (37 GHz, two orthogonal polarizations) on Nimbus 6.

The limitation on the number of channels in the earlier microwave radiometers has been overcome by the Scanning Multichannel Microwave Radiometer (SMMR) borne on Seasat and Nimbus 7, which can

measure brightness temperatures in two orthogonal planes of
polarization at five frequencies (6.63, 10.7, 18, 21, and 37 GHz).
The potential for making improved rainfall rate estimates based on
measurements in the new SMMR channels will be demonstrated.

2. The Radiative Transfer Cloud Model

A numerical model is developed to quantitatively describe the
transfer of microwave radiation in precipitating clouds. The effects
of multiple-scattering and polarization are both considered in this
formulation.

In order to simplify the mathematical development, radiative
properties of the cloud medium are assumed to be uniform in any
horizontal plane. It is further assumed that the radiation field is
axially symmetric.

The extinction optical depth τ is defined

$$\tau(z) \equiv \int_0^z k_{ext}(z') \, dz' , \qquad (2-1)$$

where z is geometric depth in the cloud medium and $k_{ext}(z)$ is the
total radiative extinction per unit length.

In this paper the intensity of radiation will be expressed in
terms of the equivalent brightness temperature. If the plane
determined by the z-axis and the given radiance path of propagation
is defined as the plane of incidence, then the polarization of any
radiance may then be described in terms of a "vertical" component TB_v
and a "horizontal" component TB_h, with planes of polarization

parallel and perpendicular to the plane of incidence, respectively. The component of brightness temperature in polarization p, propagating in the direction specified by the nadir angle θ at optical depth τ, is designated $TB_p(\tau,\mu)$, where $\mu = \cos\theta$ is chosen to represent the θ dependence.

At microwave frequencies, the equation of radiative transfer may be written in the form

$$\mu\frac{dTB_p(\tau,\mu)}{d\tau} = -TB_p(\tau,\mu) + J_p(\tau,\mu), \qquad (2\text{-}2)$$

The source function $J_p(\tau,\mu)$ represents the addition of radiant energy along a given path due to atmospheric emission and scattering. In the present development it is assumed that the effect of scattering is to completely depolarize the scattered radiance. Model error resulting from this approximation is small, see Olson (1982), and the mathematical treatment is simplified. Under this assumption the energy contribution to each polarized brightness temperature component is half the total scattered energy, and so the source function can be written

$$J_p(\tau,\mu) \equiv \left[1 - \tilde{\omega}_0(\tau)\right] \cdot T(\tau)$$

$$+ \frac{\tilde{\omega}_0(\tau)}{4\pi} \int_0^{2\pi}\int_{-1}^{+1} p(\tau,\mu;\mu^{'}) \left[\frac{TB_v(\tau,\mu^{'}) + TB_h(\tau,\mu^{'})}{2}\right] d\mu^{'}. \qquad (2\text{-}3)$$

Here, $T(\tau)$ is the atmospheric temperature at level τ in the cloud, $p(\tau,\mu;\mu')$ is the phase function for single scattering, and $\tilde{\omega}_o(\tau)$ is the albedo for single scattering.

Appropriate boundary conditions are imposed by specifying both the upwelling radiance at cloud base ($\tau = \tau^*$) and the downwelling radiance at cloud top ($\tau = 0$). If the earth's surface is characterized by an emissivity $e_p(|\mu|)$ and reflectivity $r_p(|\mu|)$, then the total radiance incident on the cloud base from below is given by

$$TB_p(\tau^*,\mu) = e_p(|\mu|)T_s + r_p(|\mu|)TB_p(\tau^*,-\mu) \qquad \mu < 0 , \qquad (2-4)$$

where T_s is the earth's skin temperature. Thus, $e_p(|\mu|)T_s$ represents upwelling emission from the earth's surface, while $r_p(|\mu|)TB_p(\tau^*,-\mu)$ is that portion of the downwelling cloud radiance which has been backscattered toward cloud base.

The radiation incident upon cloud top from above is due to unpolarized sources (e.g. solar emission or cosmic background radiation), and so the brightness temperature of this radiation is constant in any plane of polarization. The upper boundary radiance condition can be written

$$TB_p(0,\mu) = TB_{ex}(\mu) \qquad \mu > 0 . \qquad (2-5)$$

where $TB_{ex}(\mu)$ will be specified in section 4. The equation of transfer 2-2, along with boundary conditions 2-4 and 2-5 constitute a

well-posed problem which is solved using the Neumann Series method; ref. van de Hulst (1980).

To evaluate the general performance of the radiative transfer model, a comparison with the model developed by Weinman and Guetter (1977) was made. In an attempt to correctly account for the effects of scattering on the polarization of radiation, Weinman and Guetter utilized the complete phase matrix for Rayleigh scattering. The assumption made in the present study is that all radiation is completely depolarized by scattering.

For a given set of cloud model parameters the upwelling brightness temperatures at cloud top were computed and compared to the brightness temperatures calculated by Weinman and Guetter (1977, Table 4). Corresponding brightness temperatures differed by at most $4°K$ (~2%), with a $1.4°K$ root-mean-square deviation over the entire set; see Olson (1982). These results suggest that the scalar phase function approximation 2-3 should not introduce serious error into the computation of upwelling intensities.

3. Specification of Atmospheric Parameters in the Radiative Transfer Model

3.1 Liquid Hydrometeors

Liquid hydrometeors may be classified according to size as cloud droplets or raindrops. Raindrop radii are typically greater than 100 μm and less than 5 mm. In order to define the extinction and scattering properties of raindrops, Mie scattering theory is employed.

Mie´s theory completely specifies the electromagnetic properties
of a raindrop as a function of its size parameter $\tilde{x} = 2\pi r/\lambda$ (r is the
drop radius and λ is the wavelength of radiation) and complex index
of refraction $\hat{m} = \hat{n} - j\hat{k}$. The complex index of refraction of any
raindrop is taken to be that of pure liquid water. The empirical
formula proposed by Ray (1972) is used here to compute the complex
indices of refraction of water at the SMMR frequencies for a range of
environmental temperatures. The Mie extinction and scattering
coefficients and phase function, $k_{ext}(\tau)$, $k_{scat}(\tau)$, and $p(\tau,\mu;\mu^{'})$,
respectively, are evaluated numerically.

The Mie parameters are integrated over the entire raindrop-size
distribution to determine the bulk electromagnetic properties of
natural rainfall. The drop-size distribution for hurricane rainfall
proposed by Merceret (1974) is utilized in this study. Power law
fits of the extinction coefficient and albedo for single scattering
($\tilde{\omega}_o = k_{scat}/k_{ext}$) as functions of rainfall rate are listed in Table
3.1 and may be compared to the results of Savage (1978).

Due to their smaller size, non-precipitating cloud droplets have
electromagnetic properties which can be adequately described by the
approximate Rayleigh theory. In addition, the effects of scattering
by cloud droplets are negligible at the microwave frequencies
considered (i.e., $k_{ext} \cong k_{abs}$, the absorption coefficient). The
extinction coefficient for cloud droplets is given by

$$k_{ext_C} = \frac{6\pi}{\rho_L \lambda} \quad Im \left\{ - \frac{\hat{m}^2 - 1}{\hat{m}^2 + 2} \right\} \cdot LWC \, , \qquad (3-1)$$

where ρ_L is the density of water (1 gm/cm^3), and LWC is the total liquid water content of the cloud droplets.

In non-precipitating cumulus clouds a typical cloud droplet liquid water content is .5 gm/m^3, with maximum values of about 1 gm/m^3. Cloud droplet extinction coefficients computed for a liquid water content of .5 gm/m^3 are listed in Table 3.2.

Radiative extinction by cloud droplets with a liquid water content of .5 gm/m^3 is comparable in magnitude to extinction by raindrops at rainfall rates of about 2 to 5 mm/hr. Even greater extinction by droplets is possible in clouds with higher liquid water content. Measurements made during aircraft penetrations into raincells of Hurricane Allen indicate typical cloud droplet ($r < 40$ μm) liquid water contents ranging from .1 to .8 gm/m^3, with a mean of about .5 gm/m^3, R. Black (1981). However, a relationship between rainfall rate and cloud droplet liquid water content has not been established.

3.2 Ice

Ice-phase hydrometeors may be present at or above the freezing level in tropical cyclones and other strongly-convective tropical systems. However, the extinction coefficients of ice particles at the SMMR frequencies are about two orders of magnitude smaller than cloud droplets of the same equivalent liquid water content.

Recent radiometric measurements in Tropical Storm Cora by Wilheit, et al. (1982) suggest that ice may only have a small effect at frequencies < 19.35 GHz. The presence of ice has been observed in 37 GHz data over midlatitude systems by Spencer, et al. (1982), but similar measurements in Cyclone Joan (Beer, 1980) show little evidence of ice.

Although the effects of ice are neglected in the present model, aircraft probe measurements by R. Black (1982) indicate the existence of significant numbers of ice particles in tropical cyclone raincells. Improved models which include an ice layer above the liquid precipitation are currently being developed by the authors.

3.3 Mixed-phase Hydrometeors

In radar studies of tropical cyclones and squall-lines a "bright-band" of high reflectivity is commonly observed below the freezing level, Battan (1973). The bright-band is caused by the back-scattering of radiation off melting ice particles.

Unfortunately, the precise structure of the melting layer is not well known. Distributions in size, shape, and phase of melting hydrometeors have not been established, and are thought to be quite sensitive to microphysical processes such as particle aggregation and breakup. As a consequence of these uncertainties, the effects of mixed-phase hydrometeors are not considered in this study.

Since significant numbers of these particles occur only in a relatively thin layer, approximately 400 m thick, their presence is not expected to greatly influence the transfer of microwave radiation

in tropical cyclone raincells, which may extend several kilometers in height.

3.4 Molecular Absorbers

Molecular absorption is generally small at the SMMR frequencies except at 21 GHz, where water vapor extinction can be equivalent to extinction by rain for rainfall rates up to 4 mm/hr in a saturated atmosphere. The effects of molecular absorption are therefore included in the cloud model.

The model of Meeks and Lilley (1963) is used here to compute the extinction coefficient of oxygen as a function of frequency, temperature, and pressure. A number of oxygen lines between 50 and 70 GHz are broadened into a wide absorption band which extends to the SMMR frequencies. The maximum absorption occurs near the earth's surface, where relatively high pressures induce the greatest broadening effect. For water vapor the model described by Staelin (1966) is used to calculate the extinction coefficient as a function of frequency, pressure, temperature, and vapor density. The absorption spectrum of water vapor at the microwave frequencies results mainly from the rotational transition line at 22.235 GHz. The amount of absorption varies in proportion to the concentration of vapor (or relative humidity).

3.5 The Mean Tropical Cyclone Profile

Basic height profiles of temperature, pressure, and humidity
which represent average conditions in tropical cyclone raincells are
selected for use in the radiative transfer model. Such profiles were
obtained as a function of radius from the storm center by Gray and
Frank (1977) to produce the mean profiles of Table 3.3. The mean
profiles of pressure and temperature were compared to soundings
obtained in individual tropical cyclones of differing intensities by
Olson (1982). Despite differences in storm intensity, the
temperatures measured in the individual storms deviated from the
composite temperature at each pressure level by only $\pm 3^{\circ}$K on average.

At nearly all pressure levels in the tropical cyclone, a
decrease in temperature with increasing radius is observed, however,
the falloff in temperature is very gradual outside the eye-eyewall
region (i.e., at radii greater than $\sim .3^{\circ}$). The rad = 2° composite
pressure/temperature profile is therefore selected for use in the
radiative transfer model to represent mean atmospheric conditions
between $.3^{\circ}$ and 4° radius. Since nearly all tropical cyclone
rainfall occurs within a radius of 4° or 5°, profiles at greater
distance from the storm center need not be considered.

Observed temperatures in the eye-eyewall region (rad < $.3^{\circ}$) can
vary significantly from storm to storm, and so
modeling of the atmosphere in this region is not attempted.

Further it is assumed that the rad = 2° composite profile of specific humidity represents the mean vertical distribution of water vapor in the tropical cyclone atmosphere between .3° and 4° radius. Specific humidities at each pressure level deviate from the rad = 2° value by only ~±1 gm/kg over the .7° - 4° band (see Table 3.3).

In the cloudy atmosphere of active raincells or in the eyewall region (rad < .3°), the composite specific humidity is best represented by the saturation specific humidity, $q_s(T)$, at all levels where cloud is present (see Table 3.3, rad = 2° column).

The resulting pressures, temperatures, and specific humidities at designated heights in the rad = 2°, mean tropical cyclone atmosphere are listed in Table 3.4. The heights listed were determined using the hydrostatic relationship, and serve as primary data levels in the radiative transfer model. At each level the electromagnetic properties of the atmosphere are represented by the total extinction coefficient, which is the sum of the extinction coefficients of the individual atmospheric constituents, and the scattering coefficient and phase function of the raindrops.

The extinction coefficients of molecular oxygen and water vapor are completely determined by the specification of pressure, temperature, and specific humidity in the mean tropical cyclone profile. The concentration and height distribution of raindrops or cloud droplets is varied in certain model tests, but the electromagnetic properties of individual drops are completely

determined by the complex index of refraction of water at a given level temperature.

4. Specification of Boundary Conditions in the Radiative Transfer Model

The skin temperature T_s, emission coefficient $e_p(|\mu|)$, and reflection coefficient $r_p(|\mu|)$ of the lower boundary surface must be specified in the radiative transfer model. Since most tropical cyclone activity occurs in oceanic regions, specification of these boundary parameters at the sea surface is of primary importance.

A mean climatological value of sea surface temperature, 300.2°K (27°C), for the month of August in the tropical North Atlantic is selected as a representative skin temperature in the model; ref. Sverdrup, Johnson, and Fleming (1942). The most significant deviations from this mean value would be caused by storm-generated upwelling, which can cool the ocean's surface layer by ~3°K, P. Black (1981). However, the upwelling effect is generally limited to a 50 km wide strip along the storm track, and is not considered in the present development.

Numerous studies have been performed in attempts to determine the emission and reflection coefficients of the ocean's surface under different environmental conditions; Saxton and Lane (1952), Stogryn (1967, 1972), Webster, et al. (1976). These authors have considered sea surfaces altered by wind-generated foam and waves. In addition, Olson (1982) has examined the effect of raindrop impaction on the reflectivity of a water surface.

As a limiting case, the emitting and reflecting properties of a perfectly flat sea surface are first considered. The properties of such a surface are computed from the Fresnel relations; Stogryn (1967). Upon choosing mean climatological values of surface temperature (300.2°K) and salinity (36.5 parts per thousand) for the tropical North Atlantic during August, ref. Sverdrup, Johnson, and Fleming (1942), the complex dielectric constants of sea water at the SMMR frequencies are computed from Klein and Swift's (1977) algorithm. Plane surface reflection coefficients corresponding to these dielectric constants are presented in Table 4.1. The associated plane surface emission coefficients can be easily obtained using the energy conservation condition, $e_p(|\mu|) = 1 - r_p(|\mu|)$.

Variations in sea state can produce changes in surface reflection or emission. It has been demonstrated by Olson (1982) that the most significant modifications of sea surface reflectivity in the tropical cyclone environment are due to wind-generated foam and raindrop impaction.

Wilheit (1979) noted a general decrease in sea surface reflectivity from the plane surface value due to wind-generated foam. The change in reflection coefficient can be approximated by

$$\Delta r_p(|\mu|)_{foam} \cong \begin{cases} 0 \text{ , } U_{20} < 7 \text{ m/sec} \\ \\ -.006 \text{ sec/m } \cdot (1 - \exp[-\nu/7.5 \text{ GHz}]) \cdot (U_{20} - 7 \text{m/sec}) \text{ ,} \\ U_{20} > 7 \text{m/sec} \end{cases} \quad (4\text{-}1)$$

where ν is the frequency of radiation in GHz, and U_{20} is the 20 meter

wind speed in m/sec. The reflectivity change is assumed to be independent of polarization and nadir angle.

Surface reflectivity departures at the SMMR frequencies due to wind-generated foam are listed in Table 4.1. Maximum reflectivity departures of approximately -.2 to -.3 are attributed to the foam effect at a 20 m wind speed of 60 m/sec. The figures in the table corresponding to wind speeds greater than 30 m/sec should be regarded with caution, however, since they represent an extrapolation of empirical relaionships which were formulated on the basis of observations at lower wind speeds.

The effect of rain impaction on the reflecting/emitting properties of a water surface has also been investigated. In an experiment conducted at the NASA/GSFC facility (Greenbelt, Maryland), a three-band radiometer system was employed to measure the upwelling microwave radiances reflected and emitted by a droplet-roughened pond surface. Details of this experiment are described in Olson (1982). Estimated reflectivity departures due to rain impaction at an equivalent rainfall rate of 220 mm/hr are listed in Table 4.1.

The figures indicate a reduction in water surface reflectivity (negative departures) due to rain impaction at all SMMR frequencies, with departure magnitudes increasing with frequency. The greatest reflectivity departure, $\Delta r_{v,h-rain}$ = -.099 at 37 GHz, is comparable in magnitude to the foam-induced departure at intermediate wind speeds (~30 m/sec). The rain-induced departure represents an extreme

case effect, however, because of the high rainfall rate simulated in the NASA experiment.

In tropical cyclones the foam effect will most likely predominate over the rainfall impaction effect because wind speeds are very high over most of the storm area, while intense rainfall occurs mainly in limited regions of strong convection.

Only the contribution of the cosmic microwave background to the total downwelling radiance at the upper boundary of the radiative transfer model is considered. The microwave background is an essentially isotropic, unpolarized radiation field with a 2.7°K blackbody spectrum.

5. Model Results

The brightness temperature of microwave radiation at each SMMR frequency emerging from the top of a tropical cyclone raincell is computed as a function of varying model input parameters. All cloud-top brightness temperatures appearing in the tables and figures of this section are computed for the SMMR viewing angle, which corresponds to a nadir angle of 130° (50° from zenith).

5.1 The Basic State

Changes in the model inputs are made in reference to a basic state which represents the unperturbed ocean/atmosphere system. A cloudless atmosphere is assumed in this state, with profiles of pressure, temperature, and specific humidity designated by the mean cyclone profile in Table 3.4. The absorption spectra of molecular

oxygen and water vapor, which depend only upon the ambient pressure, temperature, and specific humidity (see section 3.4) are therefore completely specified in the basic state atmosphere.

Also in the basic state, the underlying ocean is assumed to be calm (plane surface), and have a skin temperature of 300.2°K (27°C). Surface reflection coefficients for these conditions have been derived using the Fresnel relations (see Table 4.1). The surface reflection coefficients may be depressed due to the influence of raindrop impaction or foam, but the skin temperature is preserved at a constant 300.2°K.

To the basic state atmosphere may be added cloud and precipitation droplets, as well as additional water vapor, but the primary profiles of pressure and temperature are maintained in all model tests.

5.2 The Variation of Cloud-top Brightness Temperature with Rainfall Rate and Precipitation Column Height

In the following model computations, layers of precipitation-size drops are added to the basic state atmosphere. The rainfall rate, or equivalently, the precipitation liquid water content is assumed to be uniform within the precipitation layer boundaries.

Radar observations of fully developed tropical cyclone raincells outside the eyewall region indicate columns of precipitation which extend from the surface to near or just above the freezing level (5 to 6 km height), P. Black (1981). Significant quantities of

precipitation-size drops reach greater heights only in the strong updrafts of the eyewall.

To simulate raincells of various heights (or cells in different stages of development), precipitation layers of differing thicknesses are tested at each rainfall rate. In each case a uniform layer of precipitation is added to the basic state atmosphere between the surface and "column height" H, where H can be 3.8, 4.8, 5.8, or 6.8 km. These heights were chosen because of their relative displacement from the freezing level, which occurs at a height of 4.8 km.

The reflectivity departures measured during the NASA experiment (see Table 4.1) are added to the basic state reflection coefficients to obtain appropriate reflection coefficients for this model experiment.

$$r_{p-rain} = r_{p-plane} + \Delta r_{p-rain} \qquad (5-1)$$

Although the experimentally-derived reflectivity departures, Δr_{p-rain}, were induced by droplet impaction at an unusually high rainfall rate, the resulting disturbed-surface reflection coefficients (r_{p-rain}) are still likely to be more realistic than the plane surface values. Indeed, similar departures are induced by the action of surface wind stress when the 20-meter wind speed is approximately 30 m/sec (see section 4).

Model-generated cloud-top brightness temperatures at 6.63, 10.7, 18, and 37 GHz are plotted as functions of rainfall rate in Figs. 5.1 through 5.8; see also Olson (1982). The 21 GHz brightness temperatures are not significantly different from those at 18 GHz.

The qualitative behavior of the brightness temperature curves can be explained in terms of the relative importance of absorption and scattering in the precipitation layer. At low rainfall rates the absorbing effect of the precipitation layer predominates. As the rainfall rate and total optical depth of the layer increase, less of the relatively low intensity surface emission (on the order of 150°K brightness temperature) is transmitted. The surface component is replaced by higher intensity cloud emission (the mean cloud temperature is approximately 285°K). The resultant cloud-top brightness temperature therefore increases with rainfall rate.

The cloud-top brightness temperature continues to increase with rainfall rate until the precipitation layer becomes so radiatively opaque that only radiation emitted near the top of the layer is transmitted to space. The maximum cloud-top brightness temperature is nearly the same as the air temperature at the top of the precipitation column.

As the absorption effect produces smaller and smaller changes in brightness temperature, the previously minor effect of scattering by raindrops begins to predominate, causing the brightness temperature to decrease. The brightness temperature decreases because the upwelling cloud emission is diluted by backscattered, low intensity

radiances from space. As the rainfall rate increases, the proportion
of larger drops, which scatter more efficiently, also increases (see
section 3.1). Thus the brightness temperature continues to decrease
as the rainfall rate, and the magnitude of the scattering effect,
increase.

Finally, it may be noted that the brightness temperature in the
vertical polarization is generally greater than the brightness
temperature in the horizontal polarization at any given frequency,
column height, and rainfall rate. This is due to the influence of
surface emission, which is always greater in the vertical
polarization at any frequency. The effect of scattering by raindrops
tends to depolarize the cloud-top radiances.

5.3 The Variation of Cloud-top Brightness Temperature with Surface Reflectivity/Emissivity

In this section, cloud-top brightness temperatures are generated
for different sea surface reflectivities and rainfall rates, while
other physical parameters are maintained at constant values.

The action of wind-generated foam is expected to produce the
greatest range of sea surface reflectivity values under storm
conditions. Reflectivity departures derived from Wilheit's (1979)
foam model are used to compute appropriate reflection coefficients
for various wind speeds.

$$r_{p-foam} = r_{p-plane} + \Delta r_{p-foam} \qquad (5-2)$$

In particular, surface reflectivities corresponding to 20-meter wind speeds of 0, 20, 40, and 60 m/sec are considered (see Table 4.1). As in the last section, a layer of precipitation-size drops is added to the basic state atmosphere; however, the precipitation column height is fixed at a typical value of 5.8 km. Computed cloud-top brightness temperatures at 6.63, 10.7, 18, and 37 GHz are plotted versus rainfall rate in Figs. 5.9 through 5.16, see also Olson (1982).

The effect of wind stress is to increase the cloud-top brightness temperature over its calm surface value (U_{20} = 0 m/sec). The contribution of surface emission to the upwelling cloud-top radiance is enhanced due to wind-generated foam, and so the resultant brightness temperature increases.

As the rainfall rate increases, and the precipitation layer becomes more radiatively opaque, less of the surface emission is transmitted by the cloud. Since the radiative extinction by raindrops at a given rainfall rate increases substantially with frequency, the effect of varying surface emission (or wind speed) on the resultant upwelling brightness temperatures is greatly diminished at the higher microwave frequencies. Also, the upwelling brightness temperature increases almost linearly with the 20-meter wind speed at any given frequency and rainfall rate.

5.4 The Effect of Non-precipitating Cloud Droplets on Computed
Cloud-top Brightness Temperatures

Because the microwave electromagnetic properties of

non-precipitating cloud droplets are accurately described by the

Rayleigh approximation (see section 3.1), only the total liquid water

content of the droplets must be known to specify the appropriate

extinction coefficients. Recent measurements by Sax and Keller

(1978) and R. Black (1981) indicate average cloud droplet liquid

water contents of .5 gm/m^3, which are roughly uniform with height and

only very gradually decrease above 1500 m (+8.5^{o}C).

To approximate conditions which might be found in non-precipita-

ting tropical cyclone clouds, cloud droplet layers with a uniformly

distributed liquid water content of .5 gm/m^3 are added to the basic

state atmosphere. The droplet layers are assumed to extend from the

surface to 3.8, 4.8, 5.8, 6.8, 7.3, and 9.5 km, covering a wide range

of layer thicknesses. Water vapor is also added to the mean profile

until the atmosphere is saturated at all levels. The underlying

ocean surface is characterized by the "precipitation-roughening"

reflection coefficients (Eq. 5-1) in order to directly compare the

model results with those derived for precipitating clouds in section

5.2.

Computed cloud-top brightness temperatures are plotted as

functions of cloud-top height in Figs. 5.17 through 5.20; see also

Olson (1982).

The cloud-top brightness temperature increases almost linearly with cloud top height at 6.63, 10.7, and 18 GHz. At 37 GHz, however, the average extinction by cloud droplets is large enough for significant reabsorption of radiation near the cloud top to occur. Therefore, the effect of increasing absorption by the entire cloud layer, which initially raises the brightness temperature, is eventually balanced by the concurrent lowering of the effective emitting temperature of the cloud as the air temperature at cloud top decreases. The net result is a brightness temperature curve which first rises and then falls as the cloud top height is increased (Fig. 5.20).

Given a particular cloud layer thickness and polarization, the brightness temperature increases with frequency, which is due to greater absorption by cloud droplets at the higher frequencies (see Table 3.2).

Usually the intensity emerging from the tops of non-precipitating clouds is less than that which emerges from columns of precipitation, except at low rainfall rates. Comparing Figs. 5.17 - 5.20 with Figs. 5.1 - 5.8, it is evident that the upwelling intensity at the top of the 5.8 km thick cloud droplet layer is approximately equal to the intensity emerging from a precipitation layer of the same thickness at rainfall rates of 4, 3, and 3 mm/hr at 6.63, 10.7, and 18 GHz, respectively. An exception to the general intensity relationship occurs at 37 GHz, where the upwelling brightness temperature at the top of the 5.8 km cloud droplet layer is at least

5°K greater than the corresponding precipitation layer brightness temperature at any rainfall rate. This result is explained by the prominent effect of scattering in the rain layer at 37 GHz, which lowers the resultant brightness temperature significantly. It should be noted, however, that non-precipitating clouds of smaller liquid water content (LWC $<.5$ gm/m^3) would necessarily absorb less radiation, and therefore the brightness temperatures upwelling from these clouds would generally be less than the temperatures plotted in Figs. 6.17 - 6.20. In this case brightness temperatures upwelling from both precipitating and non-precipitating clouds at 37 GHz could be comparable.

6. Analytical Formulae for Representing Model Output

In the analysis to follow it will be particularly convenient to work with simple analytical expressions for the brightness temperature curves produced in section 5. Specifically, brightness temperatures will be expressed as explicit functions of R, the rainfall rate; H, the precipitation column height, and r_p, the surface reflectivity.

At relatively low rainfall rates, where brightness temperature generally increases with rainfall rate, an adequate representation of the brightness temperature curves may be obtained using a single-layer, isothermal, absorbing atmosphere model. In this approximation, a simple expression for the cloud-top intensity at nadir angle $\theta_o = \cos^{-1} \mu_o$ can be derived.

$$TB_p^O(0, \mu_o) = [1 - r_p(|\mu_o|)] \cdot T_s \cdot e^{\tau_{atm}/\mu_o}$$

$$+ T_{atm} \cdot (1 - e^{\tau_{atm}/\mu_o}) \cdot [1 + r_p(|\mu_o|)e^{\tau_{atm}/\mu_o}]$$

$$+ TB_{ex}(-\mu_o) \cdot r_p(|\mu_o|) \cdot e^{2\tau_{atm}/\mu_o} . \qquad (6-1)$$

Here, T_{atm} and τ_{atm} are the temperature and total optical depth, respectively, of the single-layer model atmosphere. The extinction coefficient for rainfall is assumed to vary in proportion to a fixed power of the rainfall rate.

$$\tilde{k}_{ext_R} = A \cdot R^\alpha \qquad (6-2)$$

Paramters A and α are fitted constants, to be specified later. The total optical depth of the atmosphere then becomes

$$\tau_{atm} = [\tilde{k}_{ext_R} + \tilde{k}_{ext_C}] \cdot H + \tau_{mol} , \qquad (6-3)$$

where $\tilde{k}_{ext_C}$ is a bulk extinction coefficient for non-precipitating cloud droplets, τ_{mol} is the total optical depth of molecular absorbers, and H is the height of the precipitation column.

It is further assumed that the effective thermodynamic temperature of the absorbing atmosphere is a linear function of precipitation column height.

$$T_{atm} = T_1 + T_2 \cdot H \qquad (6-4)$$

The parameters T_1 and T_2 are fitted constants.

At 18 and 37 GHz, the effect of droplet scattering predominates at moderate to high rainfall rates, and brightness temperatures generally decrease slowly with increasing rainfall rate. The single-layer, absorbing atmosphere model fails to provide a good fit to the computed cloud-top brightness temperatures at these frequencies and rainfall rates. The decaying portions of the brightness temperature curves can be well-represented, however, by the form of an exponential with a linear correction.

$$TB_p^{'}(0,\mu_o) = G \cdot e^{-D \cdot R} + T_3 + T_4 \cdot H \qquad (6-5)$$

The parameters G, D, T_3 and T_4 are fitted constants. The surface reflection coefficient, $r_p(|\mu_o|)$, does not appear in expression 6-5, because it was demonstrated in section 5.3 that the cloud-top brightness temperature is essentially independent of changes in surface reflectivity at sufficiently high rainfall rates at 18 and 37 GHz.

Expression 6-5 is fit to computed brightness temperatures which correspond to rainfall rates between 24 and 64 mm/hr at 18 GHz, or to rainfall rates between 8 and 64 mm/hr at 37 GHz. Expression 6-1 is fit to the remaining portions of the brightness temperature curves at these frequencies, as well as the entire curves at 6.63 and 10.7 GHz. At 18 and 37 GHz the transition between the fitted functions 6-1 and 6-5 is made smooth by interpolating linearly between the functions in

the rainfall rate intervals 20 – 28 mm/hr (18 GHz) and 4 – 8 mm/hr (37 GHz). In these intervals the brightness temperature curves are represented by

$$TB_p''(0,\mu_o) = \left\{\frac{R_U - R}{R_U - R_L}\right\} \cdot TB_p^o(0,\mu_o) + \left\{\frac{R - R_L}{R_U - R_L}\right\} \cdot TB_p'(0,\mu_o) , \quad (6\text{-}6)$$

where R_U is the upper bound of the rainfall rate interval, R_L is the lower bound, $TB_p^o(0,\mu_o)$ is given by Eq. 6-1 and $TB_p'(0,\mu_o)$ by Eq. 6-5.

By employing a non-linear regression procedure, the parameters A, α, T_1, T_2, or G, D, T_3, T_4 which produce the minimum mean square deviation between the model-computed brightness temperatures and those derived from the analytical expressions 6-1 or 6-5 can be determined. In this manner the analytical expressions are fit to the family of brightness temperature curves at each frequency and polarization in the precipitation column height study of section 5.2. Of course, the surface reflection coefficients were held fixed at the "precipitation-roughening" values (see section 4) in that particular model experiment. The reflection coefficient $r_p(|\mu_o|)$ in Eq. 6-1 is therefore set equal to the appropriate "precipitation- roughening" value at $\mu_o = \cos 130^o$. Model-computed brightness temperatures corresponding to other surface reflectivities are not included in the fitting procedure, because the observed linear relationship between brightness temperature and surface reflectivity is already

well-represented in the analytical expression 6-1, and is not affected greatly by the choice of fitting parameters.

The best-fit parameters A, α, T_1, T_2, and G, D, T_3, T_4 for each frequency and polarization are listed in Table 6.1, along with the root-mean-square brightness temperature deviation between the model-computed and fitted points. The root-mean-square deviations, on the order of 1 to 2 ^{O}K, are quite small, indicating that the analytical curves provide reasonable fits to the actual model-computed points.

7. The Estimation of Rainfall Rates by Statistical Analysis of Cloud-top Brightness Temperatures

The unknown geophysical parameters of primary importance in the general inversion problem are the rainfall rate, precipitation column height, and surface reflectivity. The surface reflectivity is both frequency and polarization-dependent, and it also varies in response to changes in surface wind stress and rain impaction. In the context of a tropical cyclone it is reasonable to assume that changes in surface reflectivity would be primarily due to variations in wind stress (see section 4). Thus Wilheit's formula (Eq. 4-1) can be used to replace surface reflectivity with a more general parameter, the 20-meter wind speed, which is independent of the frequency and polarization of the radiation considered. The number of unknown geophysical parameters is thereby reduced from ten to the following three: rainfall rate, precipitation column height, and 20-meter wind speed. An attempt will be made to ascertain the functional dependence of each of these variables on the SMMR brightness

temperature measurements at 6.63, 10.7, 18, and 37 GHz in both vertical and horizontal polarizations (a total of eight separate channels).

A statistical approach to the inversion problem is utilized in the present study. Each dependent variable (geophysical parameter) is expressed as a linear combination of the independent variables (brightness temperature measurements),

$$R = a_0 + \sum_{i=1}^{n} a_i \, TB_i \qquad (7-1)$$

$$H = b_0 + \sum_{i=1}^{n} b_i \, TB_i \qquad (7-2)$$

$$U_{20} = c_0 + \sum_{i=1}^{n} c_i \, TB_i \, , \qquad (7-3)$$

where the subscripted variables a_i, b_i, and c_i are adjustable coefficients. The coefficients which yield the best-fit relationship (in the mean square sense) between the dependent and independent variables are determined by the method of step-wise regression; see Draper and Smith (1981).

The form of the equations (7-1 to 7-3) suggests that a good fit to any sensor data might only be obtained where the relationship between the geophysical parameters and cloud-top brightness temperature is linear. Unfortunately the relationship between rainfall rate, which is the parameter of greatest interest here, and brightness temperature is generally non-linear, except at 6.63 GHz (see Figs. 5.1 - 5.8). This problem is overcome by performing separate regression analyses over the rainfall rate intervals 0 - 4

mm/hr, 4 - 8 mm/hr, 8 - 16 mm/hr, 16 - 24 mm/hr, 24 - 32 mm/hr, and 32 - 64 mm/hr. Over these intervals the response of cloud-top brightness temperature to changes in rainfall rate is approximately linear in any channel. For simplicity, regression fits for precipitation column height and 20-meter wind speed are also performed over the same rainfall-rate intervals.

Ideally, a large data set consisting of microwave sensor measurements over several tropical cyclones with coincident surface observations of rainfall rate, precipitation column height, and 20-meter wind speed should be employed in the regression analysis.

An alternative approach, which is utilized here, is to create a synthetic data set based on the output of the radiative transfer cloud model. Given a rainfall rate, precipitation column height, and 20-meter wind speed, the corresponding cloud-top brightness temperatures at 6.63, 10.7, 18, and 37 GHz in both polarizations can be generated using the analytical expessions developed in section 6 (see Eqs. 6-1, 6-5, and 6-6). What remains to be determined are realistic distributions of R, H, and U_{20} values which might typically occur in a tropical cyclone.

Since separate regression analyses are performed over six distinct intervals in the 0 - 64 mm/hr range, the imposition of a rainfall rate distribution over this range would be meaningless. Instead, rainfall rates are uniformly distributed on each of the six rainfall rate intervals. Likewise, precipitation column heights are distributed uniformly between typical limits of 3.8 and 6.8 km.

It is assumed that wind speeds are distributed radially by

$$U_{20}(\text{rad}) = 60 \text{ m/sec} \cdot \left[\frac{20 \text{ km}}{\text{rad}}\right]^{.5}, \qquad \text{rad} > 20 \text{ km} \qquad (7\text{-}4)$$

as suggested by Riehl (1954, p. 288).

Various radii, and therefore wind speeds, are selected on the assumption that storm observations are uniformly distibuted over the area between radii of 20 and 450 km. In this radial band 20-meter wind speeds will range from 13 to 60 m/sec by Eq. 7-4, and consequently the relationship between surface reflectivity and wind speed is linear (see Eq. 4-1).

The various combinations of R, H, and U_{20} values are randomly generated, ignoring any possible correlations between the variables. Fifty sets of these parameters are produced for each rainfall rate interval, along with the corresponding cloud-top brightness temperatures in the eight SMMR channels. In computing the cloud-top brightness temperatures it is assumed that the model atmosphere contains no non-precipitating cloud droplets, and that the distribution of water vapor is characterized by the mean tropical cyclone profile (see section 3.5); i.e., cloud-free conditions prevail. The effect of adding clouds to the model atmosphere is examined at the end of this section.

For a given set of environmental conditions, sensor measurements of brightness temperature may not agree with model-computed cloud-top brightness temperature due to instrumental error or inaccuracies in

the model formulation. To simulate the effects of these error sources in the synthetic data set, randomly-generated, Gaussian-distributed noise is added to each brightness temperature computed by the model. Three separate cases are considered, corresponding to Gaussian noise factors with standard deviations of .5°K, 2°K, and 4°K. In each case the noise has zero mean.

A noise figure of ~1°K is compatible with errors currently reported for the SMMR data. Additional errors could arise from poor sensor spatial resolution. The best resolution attained by the SMMR instrument is at 37 GHz, where a single brightness temperature measurement represents a spatial average over a ~400 square kilometer area at the earth's surface. This area must be reduced to cumulus-scale (less than 10 km x 10 km) before the measured brightness temperatures will begin to represent "cloud-top" brightness temperatures, as defined in this study. It is assumed here that the necessary resolution will be achieved, and that the residual error in the corrected brightness temperature measurements will be on the order of 5°K or less, thus falling into the range of added noise in the regression data.

The regression coefficients a_i, b_i, and c_i for which best fit expressions are obtained in each of the six rainfall rate intervals are listed in Tables 7.1 - 7.3, along with the fraction of the total variance in each geophysical parameter which is explained by the corresponding regression formula.

A true test of the regression formulae is to invert brightness temperature data, comparing the rainfall rates, precipitation column heights, and 20-meter wind speeds derived from the regression formulae with those observed. One hundred additional combinations of rainfall rate, precipitation column height, and 20-meter wind speed are generated at random to produce cloud-top brightness temperatures via Eqs. 6-1, 6-5, and 6-6. Thus, one hundred independent "sensor observations", each consisting of brightness temperature "measurements" in the eight SMMR channels, are simulated. The various combinations of geophysical parameters, R, H, and U_{20}, which are used to generate the brightness temperatures, will serve as "ground truth" in this test.

Although values of H and U_{20} are distributed as in the regression data sets, rainfall rates are allowed to range over the full 0 - 64 mm/hr interval, following a distribution suggested by the tropical cyclone data compositing analysis of Gray and Frank (1977). The rainfall frequency distribution indicated by their figures closely fits

$$Y(R) = .105/R \qquad (7\text{-}5)$$

where Y(R) dR is the fraction of total observations where the rainfall rate is between R and R + dR.

Gaussian distributed noise at the levels prescribed in the regression data is added to the "inversion" brightness temperature data to form three test sets.

In the foregoing development, separate regression formulae were produced for each of six rainfall rate intervals. Therefore, a method for identifying the correct rainfall rate interval on the basis of the brightness temperature data alone must be included in the inversion procedure. The following method is suggested.

Initially, a rough estimate of the rainfall rate can be made using the 6.63 GHz horizontal brightness temperature "measurement". In this channel the relationship between cloud-top brightness temperature and rainfall rate is approximately linear over the entire 0 - 64 mm/hr interval (see Fig. 5.1), and so a reasonable linear regression fit

$$R = \frac{.394 \ \mathrm{mm}}{\mathrm{hr-^oK}} \cdot TB_{6.63h} - 35.0 \ \mathrm{mm/hr} \qquad (7-6)$$

to the model-computed points in the interval 4 mm/hr < R < 32 mm/hr is made for nominal conditions: H = 5.8 km; surface reflectivity is equal to the "precipitation-roughening" value.

Given the 6.63 GHz horizontal brightness temperature, a crude first guess of the rainfall rate is derived using formula 7-6. This rainfall rate will fall into one of the six rainfall rate intervals. The regression equations 7-1 to 7-3 corresponding to that particular interval are then employed, using brightness temperature

"measurements" in the eight channels, to yield estimates of rainfall rate, precipitation column height, and 20-meter wind speed.

If the new estimate of rainfall rate lies within the initial interval, then the original interval choice is assumed to be correct, and the values of R, H, and U_{20} derived from the corresponding regression equations are considered to be final "best" estimates.

If the regression estimate of rainfall rate falls into an interval other than the original rainfall rate interval, then the regression equations corresponding to the new interval are used to produce revised estimates of R, H, and U_{20}.

If the revised regression estimate of rainfall rate falls within the corresponding domain of the regression, then the revised estimates of R, H, and U_{20} are considered best estimates. Otherwise the procedure outlined in the last paragraph is repeated until the estimated rainfall rate falls within the corresponding regression interval.

The inversion procedure just described is applied to the brightness temperature test data. Each set of cloud-top brightness temperatures in the eight SMMR channels is inverted to yield estimates of R, H, and U_{20}. These parameter values can then be compared to the parameters which were used originally to generate the cloud-top temperatures. The latter set of parameters will act as "ground truth" in this test; therefore, error in a parameter estimate is defined as its deviation from the "ground truth" value.

To help clarify the analysis of the inversion results, all test cases in which the rainfall rate is less than .1 mm/hr are classified as "no rain" cases. Out of 100 test cases, 35 are classified as "non-raining" by this criterion. For the remaining 65 cases in each noise level category the root-mean-square errors in the geophysical parameter estimates are listed in Table 7.4, along with the mean "ground truth" values of the parameters.

It should be noted that the distribution of rainfall rates is somewhat biased towards low rainfall rate cases ($\bar{R}$ = 10.6 mm/hr). Nevertheless, r.m.s. errors in the rainfall rate estimates appear to be quite reasonable (~1mm/hr). In addition, there is only a modest increase in error in response to increased levels of noise in the regression/inversion brightness temperature data. This last result is important because it suggests that the retrieval of rainfall rates from the microwave brightness temperature measurements may not depend critically on the details of the cloud modeling or the precision of the sensor measurements themselves.

Specific results of the rainfall rate inversion test are represented diagrammatically in Figs. 7.1 - 7.3. The ordinate in each figure is the deviation of the estimated rainfall rate from its "surface truth" value. The deviations (discrete points) are plotted as functions of rainfall rate. For reference purposes, isopleths of percentage error are also included in these diagrams.

Although the average magnitude of errors generally increases
with rainfall rate, the percentage error in the rainfall rate
estimates tends to decrease as the rainfall rate increases. At the
σ_{noise} = 4°K level, maximum errors are close to 30% at 4 mm/hr, while
they decrease to about 15% at 64 mm/hr. This result is comparable to
the error estimate derived by Chang and Milman (1982).

Root-mean-square errors in the precipitation column height
estimates (~15% of the mean value) and 20-meter wind speed (~20%) are
also quite tolerable. The error in the wind speed estimates clearly
increases with the noise level in the regression/inversion data,
whereas the error in the column height estimates varies little and
exhibits somewhat more ambiguous behavior.

In actuality, both raindrops and non-precipitating cloud
droplets coexist in tropical cyclone raincells, but the relative
populations of these droplets in active cells is still not well
known. Nevertheless, the effect of liquid cloud droplets on the
inversion method can be studied using the single-layer, absorbing
atmosphere model (see section 6).

The height distribution of liquid cloud droplets is expected to
be roughly proportional to the height distribution of raindrops.
Therefore a bulk cloud droplet extinction coefficient, κ_{ext_C} is
proposed in order to make the total optical depth of cloud droplets,
$\kappa_{ext_C} \cdot H$, proportional to the precipitation column height. For the
purposes of this study the extinction coefficient κ_{ext_C} is defined

$$\mathcal{K}_{ext_C} = \tau_{drop}/5.8 \text{ km} \qquad\qquad (7\text{-}7)$$

Here, τ_{drop} is the total optical depth of a layer of uniformly distributed, non-precipitating liquid cloud droplets with a liquid water content of .5 gm/m^3, which extends from the surface to a height of 5.8 km in the mean tropical cyclone atmosphere (see Table 3.4). Such a layer of liquid cloud droplets is roughly consistent with aircraft probe measurements of liquid water contents in tropical cyclone raincells, R. Black (1981). The cloud droplet extinction coefficient, so defined, is introduced into the single-layer model (see Eq. 6-1).

It is also assumed that the model atmosphere is saturated, as opposed to the unsaturated "mean" tropical cyclone atmosphere. Extinction by the additional water vapor needed to saturate the atmosphere is included in the molecular optical depth term, τ_{mol}, of the single-layer model.

Aside from the alterations made in $\mathcal{K}_{ext_C}$ and τ_{mol}, all other parameters in the single-layer model are maintained at their previous values.

As in the foregoing development, synthetic brightness temperature data is generated using the fitted expressions 6-1, 6-5 and 6-6. The effects of cloud droplets are represented in these expressions except at 18 GHz with R > 28 mm/hr and at 37 GHz with R > 8 mm/hr, a deficiency which could have a significant influence on the selection and weighting of channels in the regression analysis.

Gaussian-distributed noise with zero mean and a standard deviation of $2°K$ is added randomly to brightness temperatures in each of the regression/inversion data sets.

Coefficients in the resulting regression formulae (7-1 through 7-3) are listed in Table 7.5.

Comparing the $2°K$ noise level regression equations in Table 7.5 (.5 gm/m^3 LWC cloud layer) with the corresponding expressions in Tables 7.1 - 7.3 (no cloud droplets), it may be noted that the rainfall rate and 20-meter wind speed formulae explain a smaller fraction of the variance in these parameters when cloud droplets are present in the model atmosphere. The average decrease in explained variance is small, however (~3%). Conversely, the precipitation column height formulae generally show some improvement in explaining parameter variance with the addition of the cloud layer.

As a final test of the regression formulae which were developed for the cloudy tropical cyclone atmosphere, the expressions in Table 7.5 are used to invert an independent data set of one hundred sensor observations, where each observation consists of brightness temperature "measurements" in the eight SMMR channels. The brightness temperature data is generated from the fitted expressions 6-1, 6-5, and 6-6. In order to be consistent with the regression data set, a .5 gm/m^3 LWC cloud droplet layer of thickness H is included in the saturated model atmosphere. Also, Gaussian-distributed noise having zero mean and a standard deviation of $2°K$ is added at random to the brightness temperature data.

The same inversion procedure that was applied to the "cloud-free" data is employed here. Resulting estimates of rainfall rate, precipitation column height, and 20-meter wind speed are compared to the "ground truth" values which were used to generate the brightness temperature data.

The r.m.s. errors in the rainfall rate, precipitation column height, and 20-meter wind speed estimates (not shown) are not significantly different from those in the "cloud-free" inversion estimates; see Olson (1982). Errors in the rainfall rate estimates are plotted versus rainfall rate in Fig. 7.4. The distribution of errors differs negligibly from the corresponding distribution in the "cloud-free" analysis (see Fig. 7.2).

Given the assumption that the quantity of non-precipitating liquid water (in cloud droplets) is simply proportional to the height of the precipitation column, it has been demonstrated that the inversion method can still produce reasonable estimates of rainfall rate. Data support for more elaborate parameterizations of the liquid water distribution in tropical cyclone raincells is lacking at the present time.

8. Conclusions

The radiative transfer model developed in this study has been shown to perform satisfatorily based on a comparison with the Weinman and Guetter (1977) model results. Although the partitioning of energy between the polarized components of drop-scattered radiation is simplified in the present model (energy is divided equally between

the components), the resultant upwelling brightness temperatures in a representative set of test cases differ by only $1.4 ^\circ K$ r.m.s. from the corresponding temperatures of Weinman and Guetter, who utilized the complete Rayleigh phase matrix to describe the partitioning of scattered energy. The maximum brightness temperature deviation is $4 ^\circ K$ (2%) over the entire set.

Model parameters which characterize environmental conditions within tropical cyclone raincells have been determined. In addition to absorption and scattering by raindrops, the absorption of microwave radiation at the SMMR frequencies by non-precipitating cloud droplets, molecular oxygen, and water vapor in the hurricane atmosphere is considerable. Ice particles and mixed-phase hydrometeors should have only a minor effect and are not included in the present model.

Boundary radiances in the model are characterized by the sea surface temperature and surface reflectivity (lower boundary), and the cosmic microwave background (upper boundary). The sea surface reflectivity varies considerably with surface conditions. Wind-induced foam would account for most of the variability in surface reflectivity within the hurricane environment. However, it has been demonstrated experimentally by Olson (1982) that raindrop impaction of the surface, which can lower the reflectivity by as much as ~.1 at 37 GHz, has an effect of nearly the same magnitude.

In model simulations of the microwave radiative transfer in tropical cyclone raincells over the ocean (excluding the effects of non-precipitating liquid water), cloud-top brightness temperatures at each of the SMMR frequencies 6.63, 10.7, 18, and 37 GHz increase fairly rapidly with rainfall rate until a maximum value is attained. This is followed by a relatively gradual decrease in cloud-top brightness temperature with rainfall rate which can be attributed to raindrop scattering effects.

Nominal variations in precipitation column height and sea surface reflectivity can cause significant changes in the brightness temperature versus rainfall rate relationship. Cloud-top brightness temperatures tend to increase (decrease) with increasing precipitation column height if the rainfall rate is less than (greater than) the critical value. Increases in surface reflectivity always result in diminished brightness temperatures, except in those cases where the clouds are so optically thick that the surface boundary radiances are totally obscured. In such cases, no change in brightness temperature is observed. Moreover, the response of cloud-top brightness temperature to changes in sea surface reflectivity (or 20-meter wind speed) is nearly linear at any given frequency and rainfall rate.

The brightness temperatures of 6.63, 10.7, and 18 GHz radiation emerging from a non-precipitating liquid water cloud (5.8 km thick, LWC = .5 gm/m^3) are about equal to the intensities emerging from a precipitation layer of the same thickness at rainfall rates of a few

millimeters per hour. At 37 GHz, the upwelling brightness temperature at the top of such a non-precipitating cloud is actually somewhat greater than the corresponding precipitation layer brightness temperature at any rainfall rate. In general it may be concluded, however, that the discrimination between lightly precipitating and non-precipitating clouds in satellite imagery at these frequencies might be difficult.

The radiative transfer modeling demonstrates the potential of the 6.63 and 10.7 GHz channels to provide information on tropical cyclone rainfall rates that was heretofore unavailable from sensor channels at higher microwave frequencies. Cloud-top brightness temperatures in the 6.63 GHz channels are sensitive to changes in precipitation intensity over the entire range of rainfall rates from 0 to 64 mm/hr. Brightness temperature sensitivity is observed in the 10.7 GHz channels up to a rainfall rate of ~32 mm/hr. In contrast, the response of the 18 and 37 GHz brightness temperatures to changes in rainfall rate is minimal at rainfall rates greater than 16 mm/hr.

Regression equations derived from model-generated synthetic brightness temperature data form the basis of a rainfall rate inversion method presented in section 7. The synthetic data represent a plausible set of SMMR brightness temperatures over a tropical cyclone. Actual SMMR hurricane data with coincident surface truth (rainfall rate observations) are not available at present. It is assumed in this development that individual raincells are resolved in the satellite imagery; i.e., each brightness temperature

represents an area of nearly uniform precipitation. Thus the applicability of the rainfall rate inversion method is contingent upon improvements in SMMR resolution that would allow the delineation of individual tropical cyclone raincells (less than 10 km × 10 km). The best resolution presently available is ~16 km × 25 km at 37 GHz.

Gaussian-distributed noise is added to the synthetic data in order to simulate instrumental and/or modeling errors.

Independent model-generated data sets were produced for the purpose of testing the inversion method. It is demonstrated that the inversion method can yield reasonable estimates of rainfall rate from brightness temperature measurements in the SMMR channels despite significant noise levels in the data. As Gaussian noise levels are increased from σ_{noise} = .5°K to 4°K, the r.m.s. error in rainfall rate estimates over the hurricane data set increases from .55 to 1.7 mm/hr. Although errors in individual rainfall rate estimates tend to increase with rainfall rate, percentage errors decrease as precipitation intensity increases. Maximum percentage errors decrease from ~30% at 4 mm/hr to ~15% at 64 mm/hr (σ_{noise} = 4°K case). The addition of a non-precipitating cloud droplet layer (LWC = .5 gm/m^3; thickness equal to the precipitation column height) to the model atmosphere has a negligible effect on the performance of the inversion method.

The test results suggest that the success of this statistical inversion method may not depend critically on noise levels in the brightness temperature data or errors in the modeling. The

statistical approach might also be used to make retrievals of
precipitation column height and 20-meter wind speed. Of course, the
ultimate practicability of any inversion method cannot be evaluated
without actual satellite sensor measurements and concurrent
observations of the geophysical variables in question. A coordinated
effort to measure rainfall rates and other relevant quantities such
as wind speed, sea surface temperature, and the distribution of cloud
liquid water should be implemented.

Acknowledgments

Bibliography

Allison, L.J., E.B. Rodgers, T.T. Wilheit and R.W. Fett,
1974: Tropical cyclone rainfall as measured by the Nimbus 5
Electrically Scanning Microwave Radiometer.
Bull. Amer. Meteor. Soc., 55, 1074-1089.

Austin, P.M. and S.G. Geotis, 1978: Evaluation of
the Quality of Precipitation Data from a Satellite-Borne
Radiometer. Final report under NASA grant NSG5024, Dept. of
Meteorology, M.I.T., Cambridge, MA, 33 pp.

Battan, L.J., 1973: Radar Observation of the Atmosphere. Chicago,
The University of Chicago Press, 324 pp.

Beer, T., 1980: Microwave sensing from satellites. Remote Sensing of the Environment, 9, 65-85.

Black, P., 1981: private communication - with NHRL, Coral Gables, FL.

Black, R., 1981, 1982: private communication - with NHRL, Coral Gables, FL.

Chang, A.T.C. and A.S. Milman, 1982: Retrieval of Ocean Surface and Atmospheric Parameters from Multichannel Microwave Radiometric Measurements. IEEE Transactions on Geoscience and Remote Sensing, GE-20, 217-224.

Draper, N.R. and H. Smith, 1981: Applied Regression Analysis, 2nd Edition. New York, John Wiley and Sons, 709 pp.

Gray, W.M. and W.M. Frank, 1977: Tropical Cyclone Research by Data Compositing. Naval Environmental Prediction Research Facility Technical Report TR-77-01, Monterey, CA, 70 pp.

Klein, L.A. and C.T. Swift, 1977: An improved model for the dielectric constant of sea water at microwave frequencies. IEEE Trans. Antennas Propagat., AP-25, 104-111.

Meeks, M.L. and A.E. Lilley, 1963: The microwave spectrum of oxygen in the earth's atmosphere. J. Geophys. Res., 68, 1683-1703.

Merceret, F.J., 1974: On the size distribution of raindrops in Hurricane Ginger. Mon. Wea. Rev., 102, 714-716.

Olson, W.S., 1982: Estimation of Rainfall Rates in Tropical Cyclones by Passive Microwave Radiometry. Ph.D. Thesis (in progress), Department of Meteorology, University of Wisconsin, Madison, WI.

Ray, P.S., 1972: Broadband complex refractive indices of ice and water. Applied Optics, 11, 1836-1843.

Riehl, H., 1954: Tropical Meteorology. New York, McGraw-Hill Book Company, 392 pp.

Rodgers, E.B. and R.F. Adler, 1979: Tropical Cyclone Rainfall Characteristics as determined from a Satellite Passive Microwave Radiometer. NASA Technical Memorandum 80596, NASA/GSFC, Greenbelt, MD, 43 pp.

Savage, R.C., 1978: The radiative properties of hydrometeors at microwave frequencies. J. Appl. Meteor., 17, 904-911.

Savage, R.C. and J.A. Weinman, 1975: Preliminary calculations of the upwelling radiance from rainclouds at 37.0 and 19.35 GHz. Bull. Amer. Meteor. Soc., 56, 1272-1274.

Sax, R.I. and V.W. Keller, 1978: Relationship of ice to water near -10°C within a population of Florida cumuli. Preprints of the Conference on Cloud Physics and Atmospheric Electricity, Issaquah, WA 300-305.

Saxton, J.A. and J.A. Lane, 1952: Electrical properties of sea water: reflection and attenuation characteristics at v.h.f. Wireless Engineer, 29, 269-275.

Spencer, R.W., W.S. Olson, R. Wu, D.W. Martin, J.A. Weinman, B.B. Hinton and D.A. Santek, 1983: Heavy Thunderstorms Observed over Land by the Nimbus-7 Scanning Multichannel Microwave Radiometer. (to appear in J. Appl. Meteor.).

Staelin, D.H., 1966: Measurements and interpretation of the microwave spectrum of the terrestrial atmosphere near 1-cm wavelength. J. Geophys. Res., 71, 2875-2881.

Stogryn, A., 1967: The apparent temperature of the sea at microwave frequencies. IEEE Trans. Antennas Propagat., AP-15, 278-286.

Stogryn, A., 1972: The emissivity of sea foam at microwave frequencies. J. Geophys. Res., 77, 1658-1666.

Sverdrup, H.U., M.W. Johnson and R.H. Fleming, 1942: The Oceans - Their Physics, Chemistry, and General Biology. New York, Prentice-Hall, Inc., 1087 pp.

van de Hulst, H.C., 1980: Multiple Light Scattering: Tables, Formulas, and Applications, Vol. 2. New York, Academic Press, 739 pp.

Webster, W.J., Jr., T.T. Wilheit, D.B. Ross and P. Gloersen, 1976: Spectral characteristics of the microwave emission from a wind-driven foam-covered sea. J. Geophys. Res., 81, 3095-3099.

Weinman, J.A. and P.J. Guetter, 1977: Determination of rainfall distributions from microwave radiation measured by the Nimbus 6 ESMR. J. Appl. Meteor., 16, 437-442.

Wilheit, T.T., 1979: A model for the microwave emissivity of the ocean's surface as a function of wind speed. NASA Technical Memorandum - 80278, NASA/GSFC, Greenbelt, MD, 19 pp.

Wilheit, T.T., A.T.C. Chang, J.L. King, E.B. Rodgers, R.A. Nieman, B.M. Krupp, A.S. Milman, J.S. Stratigos and H. Siddalingaiah, 1982: Microwave Radiometric Observations near 19.35, 92 and 183 GHz of Precipitation in Tropical Storm Cora. J. Appl. Meteor., 21, 1137-1145.

Wilheit, T.T., A.T.C. Chang, M.S.V. Rao, E.B. Rodgers and J.S. Theon, 1977: A satellite technique for quantitatively mapping rainfall rates over the oceans. J. Appl. Meteor., 16, 551-560.

Table 3.1 Best-fit parameters for power curve representations of tropical cyclone rainfall extinction coefficient and albedo for single scattering at 273.15°K. The coefficient of determination, w^2, for each least squares fit is also listed.

$k_{ext_R} = \Psi R^\eta$ (k_{ext_R} in km^{-1} for R in mm/hr)

Frequency[GHz]	Ψ	η	w^2
6.63	8.31×10^{-4}	1.15	.996
10.7	2.95×10^{-3}	1.14	.999
18.	1.06×10^{-2}	1.10	.999
21.	1.54×10^{-2}	1.08	1.00
37.	6.13×10^{-2}	.974	1.00

$\tilde{\omega}_o = \Lambda R^\kappa$ ($\tilde{\omega}_o$ dimensionless, R in mm/hr)

Frequency[GHz]	Λ	κ	w^2
6.63	1.22×10^{-2}	.354	.997
10.7	2.47×10^{-2}	.367	1.00
18.	6.59×10^{-2}	.346	.998
21.	9.13×10^{-2}	.311	.996
37.	2.37×10^{-1}	.159	.986

Table **3.2** Cloud droplet extinction coefficients at 273.15°K for a
total liquid water content of .5 gm/m^3.

Frequency[GHz]	$k_{ext}[km^{-1}]$
6.63	4.75×10^{-3}
10.7	1.23×10^{-2}
18.	3.42×10^{-2}
21.	4.62×10^{-2}
37.	1.33×10^{-1}

Table **3.3** Mean tropical cyclone temperature and humidity profiles (Gray and Frank, 1977).

T,q mean temperature, specific humidity

<div align="center">eye   rad = .7° (radius in degrees latitude)</div>

Pressure [mb]	T[°K]	q[gm/kg]	T[°K]	q[gm/kg]
sfc	---	---	297.6	19.4
950	298.0	19.2	297.0	18.4
900	295.2	17.1	294.2	16.8
850	293.4	15.3	292.0	15.3
800	291.8	13.8	289.8	14.0
700	287.4	10.4	284.4	11.2
600	283.2	7.8	278.2	8.2
500	275.8	4.7	270.8	6.0
400	266.0	2.8	262.0	3.5
300	252.2	1.2	249.2	1.5
250	241.8	.6	239.8	---
200	228.6	---	227.2	---
150	213.4	---	212.4	---
100	196.0	---	196.0	---

		rad = 2°			rad = 4°	
Pressure [mb]	T[°K]	q[gm/kg]	q_s[gm/kg]		T[°K]	q[gm/kg]
sfc	298.8	19.4	---		299.2	18.8
950	296.8	17.3	20.0		296.8	16.1
900	294.0	15.7	17.7		294.0	14.5
850	291.6	13.8	16.1		291.6	12.5
800	289.2	12.1	14.8		289.2	10.7
700	283.8	9.1	11.6		283.8	7.6
600	277.2	6.5	8.7		276.8	5.3
500	270.0	4.3	6.1		269.2	3.3
400	260.4	2.2	3.6		259.2	1.7
300	246.2	.8	1.4		245.0	.6
250	236.8	---	.7		235.2	---
200	224.4	---	---		223.0	---
150	209.6	---	---		208.6	---
100	197.6	---	---		196.8	---

Table 3.3 (cont.)

Pressure [mb]	rad = 8°		rad = 12°		Mean Tropical[+] Profile (Jordan, 1958)	
	T[°K]	q[gm/kg]	T[°K]	q[gm/kg]	T[°K]	q[gm/kg]
sfc	298.8	17.7	298.4	17.1	299.4	18.2
950	296.4	15.0	295.4	14.1	296.2	15.3
900	293.2	13.1	292.6	12.6	293.0	13.0
850	290.8	11.1	290.0	10.7	290.4	11.0
800	288.4	9.3	287.5	8.9	287.8	8.4
700	283.2	6.1	282.4	5.8	281.8	5.8
600	276.2	4.0	275.4	3.9	274.6	3.6
500	268.0	2.4	267.2	2.2	266.2	2.1
400	257.8	1.2	257.0	1.1	255.4	---
300	243.2	.4	242.2	.4	240.0	---
250	233.6	---	232.6	---	229.8	---
200	221.6	---	221.2	---	218.0	---
150	208.0	---	208.0	---	205.6	---
100	197.0	---	197.8	---	199.6	---

[+]mean sounding for the period July-October, 1946-1955

Table 3.4 The mean tropical cyclone profile.[+] Listed are primary data levels of the radiative transfer model, applicable to the region between radii of .3° and 4° (radius measured in degrees latitude from eye position).

Height[km]	z[km][*]	P[mb]	T[°K]	q[gm/kg]
12.3	0.00	200.4	227.0	0.00
9.48	2.79	300.2	245.2	0.80
7.34	4.93	400.8	258.4	2.20
6.78	5.48	431.1	261.6	2.85
5.79	6.48	490.0	267.4	4.09
4.79	7.48	555.8	273.2	5.53
3.78	8.49	628.9	278.8	7.25
3.24	9.03	672.0	281.8	8.37
1.65	10.6	810.7	290.2	12.5
0.00	12.3	980.2	298.8	19.4

[+]based upon the r=2° composite profile of Gray and Frank (1977).

[*]depth in the cloud model.

Table 4.1 Reflection coefficients for a plane sea surface
(T_s = 300.2 $^\circ$K, salinity = 36.5 ppt) at the SMMR frequencies.
Also listed are reflection coefficient departures due to
wind-generated foam and rain impaction.

Freq. [GHz]	Nadir Angle[o]	r_v	r_h	U_{20} [m/sec]	$\Delta r_{v,h}$ foam	$\Delta r_{v,h}$ rain (220 mm/hr)
6.63	0	.633	.633	0	.000	-.056
	10	.629	.638	10	-.010	
	20	.615	.651	20	-.046	
	30	.590	.673	30	-.081	
	40	.551	.705	40	-.116	
	50	.491	.745	50	-.151	
	60	.399	.796	60	-.187	
	70	.255	.855			
10.7	0	.625	.625	0	.000	-.062
	10	.620	.629	10	-.014	
	20	.606	.643	20	-.059	
	30	.581	.665	30	-.105	
	40	.541	.697	40	-.150	
	50	.480	.739	50	-.196	
	60	.388	.790	60	-.241	
	70	.245	.851			
18.	0	.608	.608	0	.000	-.072
	10	.604	.613	10	-.016	
	20	.589	.627	20	-.071	
	30	.564	.650	30	-.125	
	40	.523	.683	40	-.180	
	50	.461	.726	50	-.234	
	60	.368	.780	60	-.289	
	70	.228	.844			
21.	0	.601	.601	0	.000	-.076
	10	.596	.606	10	-.017	
	20	.582	.620	20	-.073	
	30	.556	.644	30	-.130	
	40	.514	.677	40	-.186	
	50	.453	.721	50	-.242	
	60	.360	.775	60	-.299	
	70	.221	.840			
37.	0	.560	.560	0	.000	-.099
	10	.555	.565	10	-.018	
	20	.539	.580	20	-.077	
	30	.512	.605	30	-.137	
	40	.469	.641	40	-.196	
	50	.405	.688	50	-.256	
	60	.313	.748	60	-.316	
	70	.184	.820			
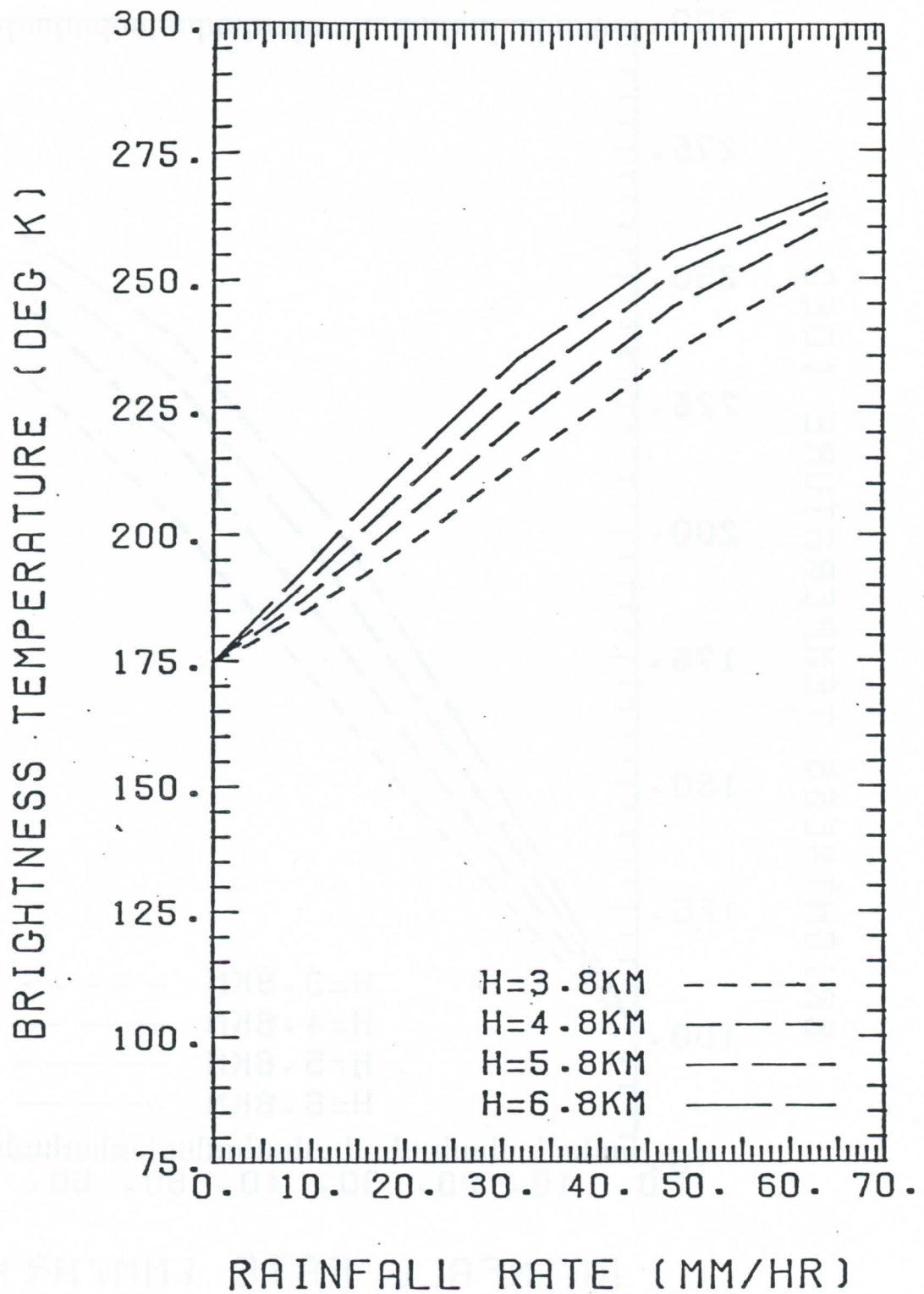
Fig. 5.1 6.63 GHz, vertical polarization.
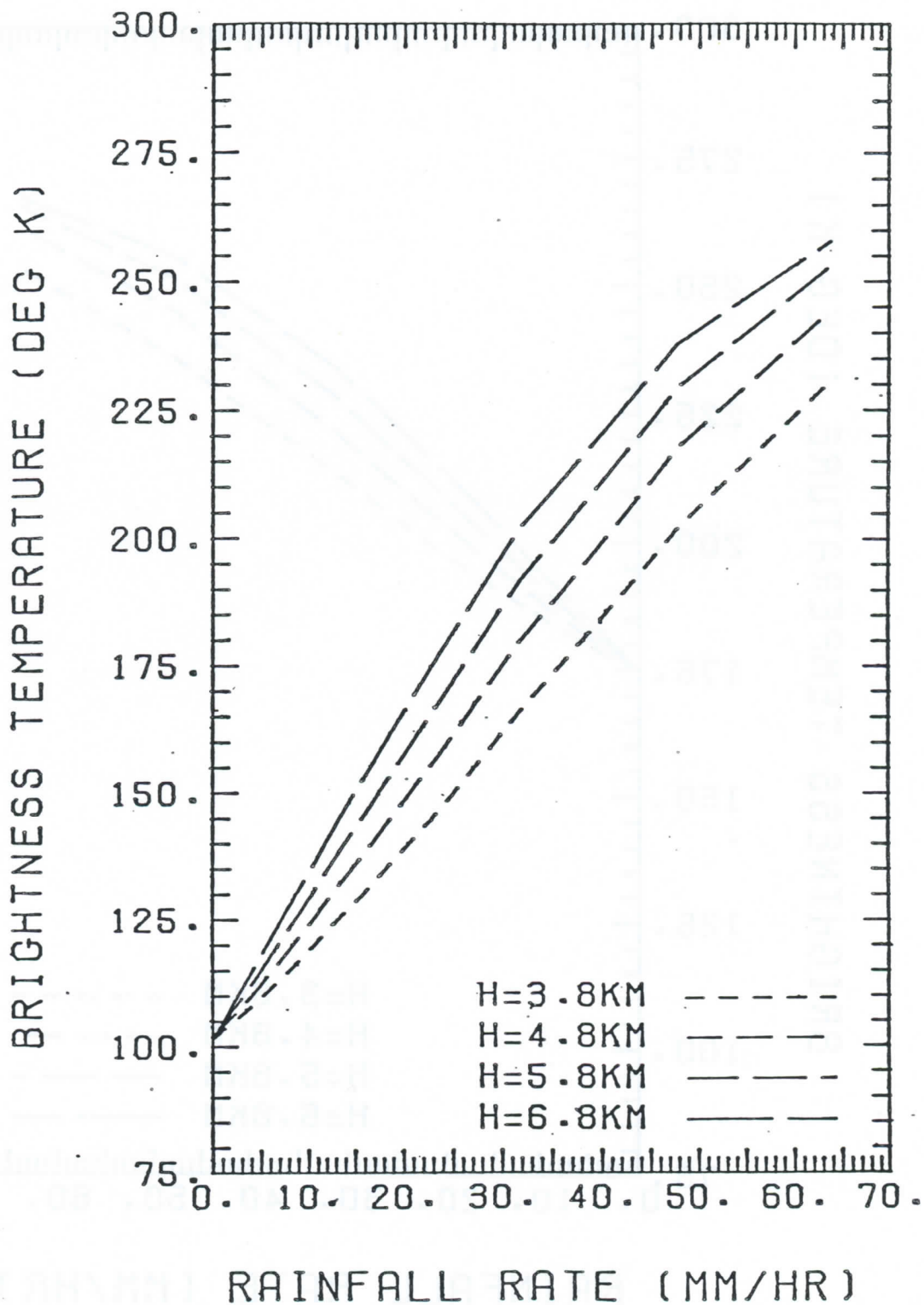
Fig. 5.2   6.63 GHz, horizontal polarization.
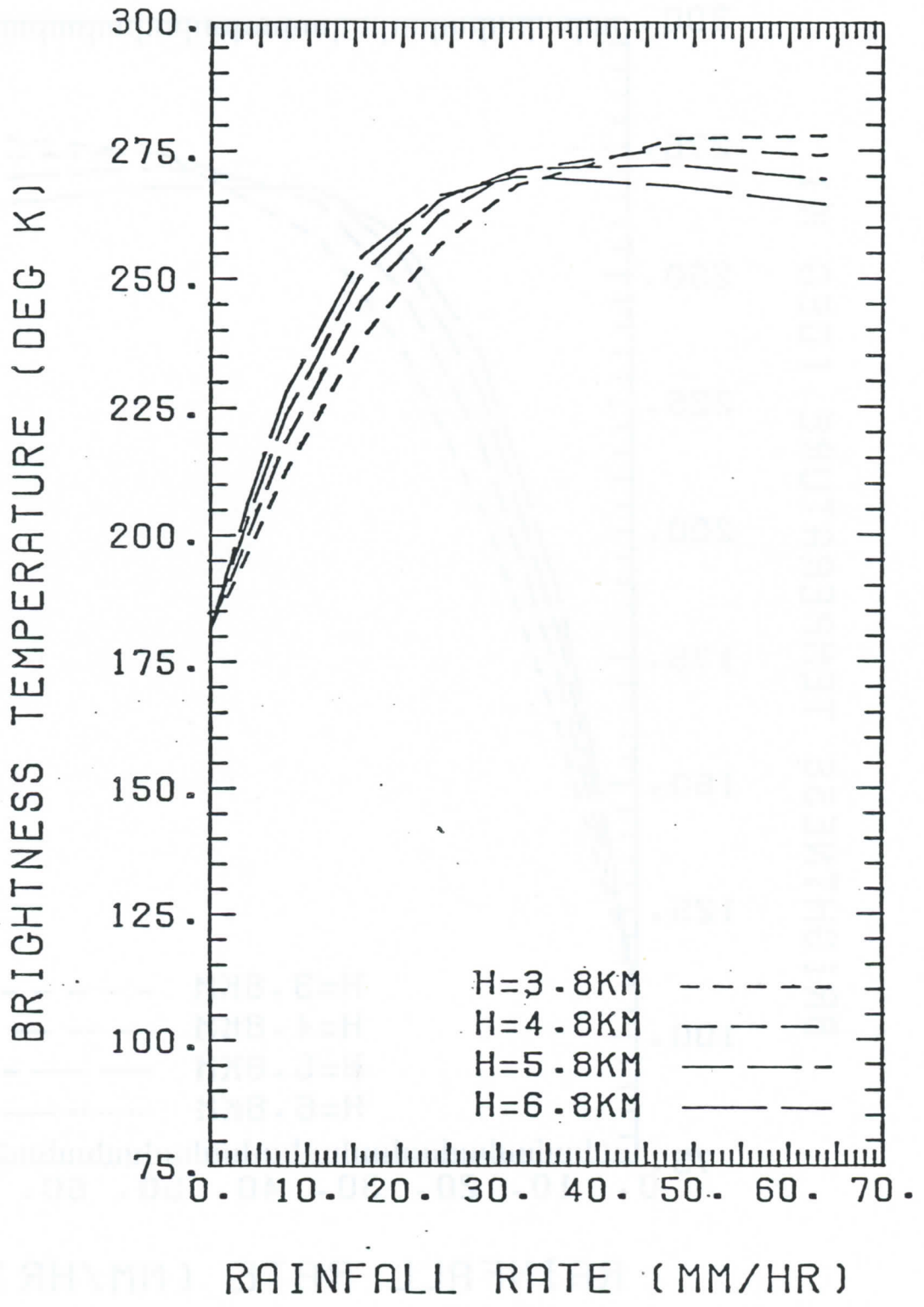
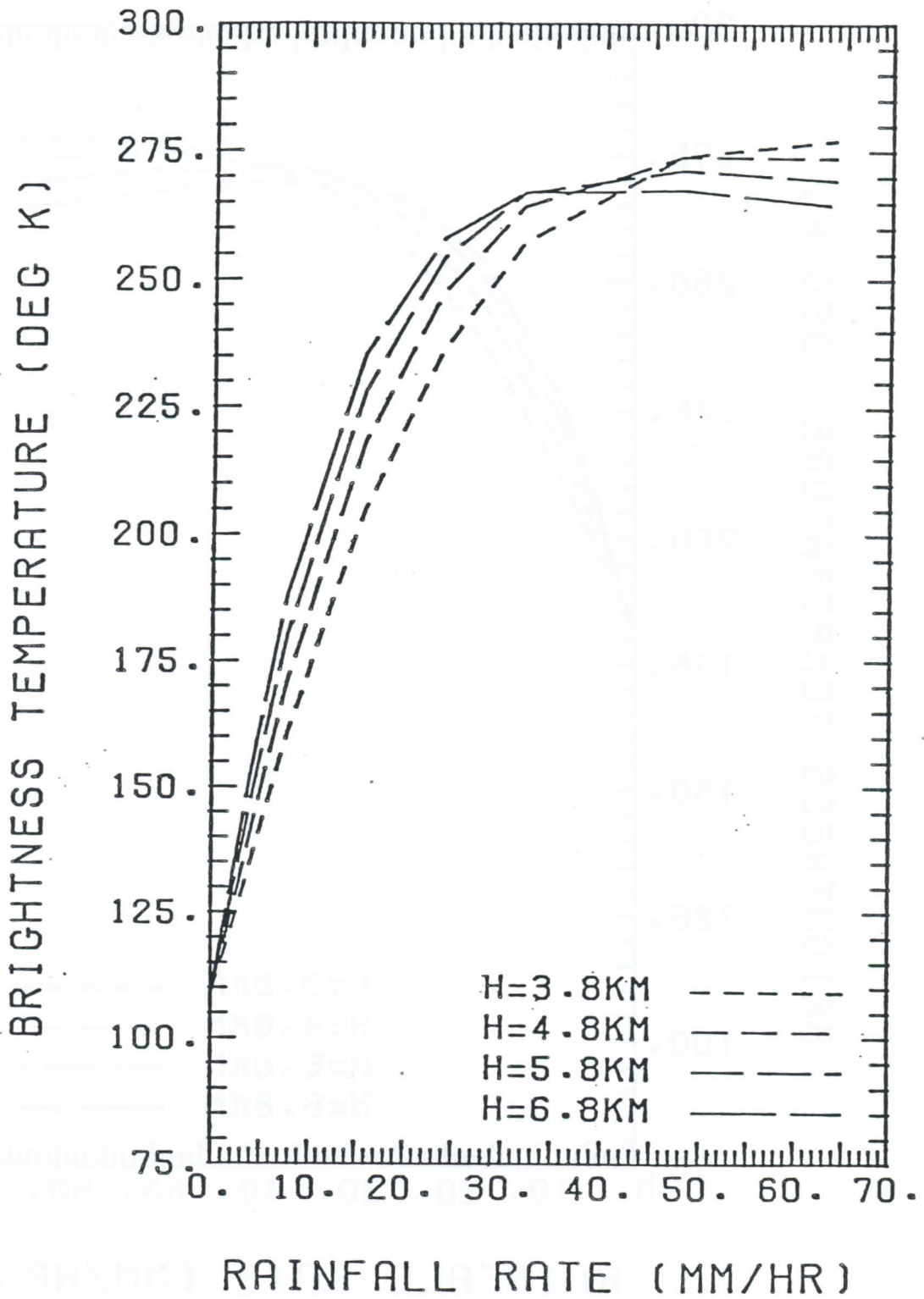Fig. 5.3 10.7 GHz, vertical polarization.

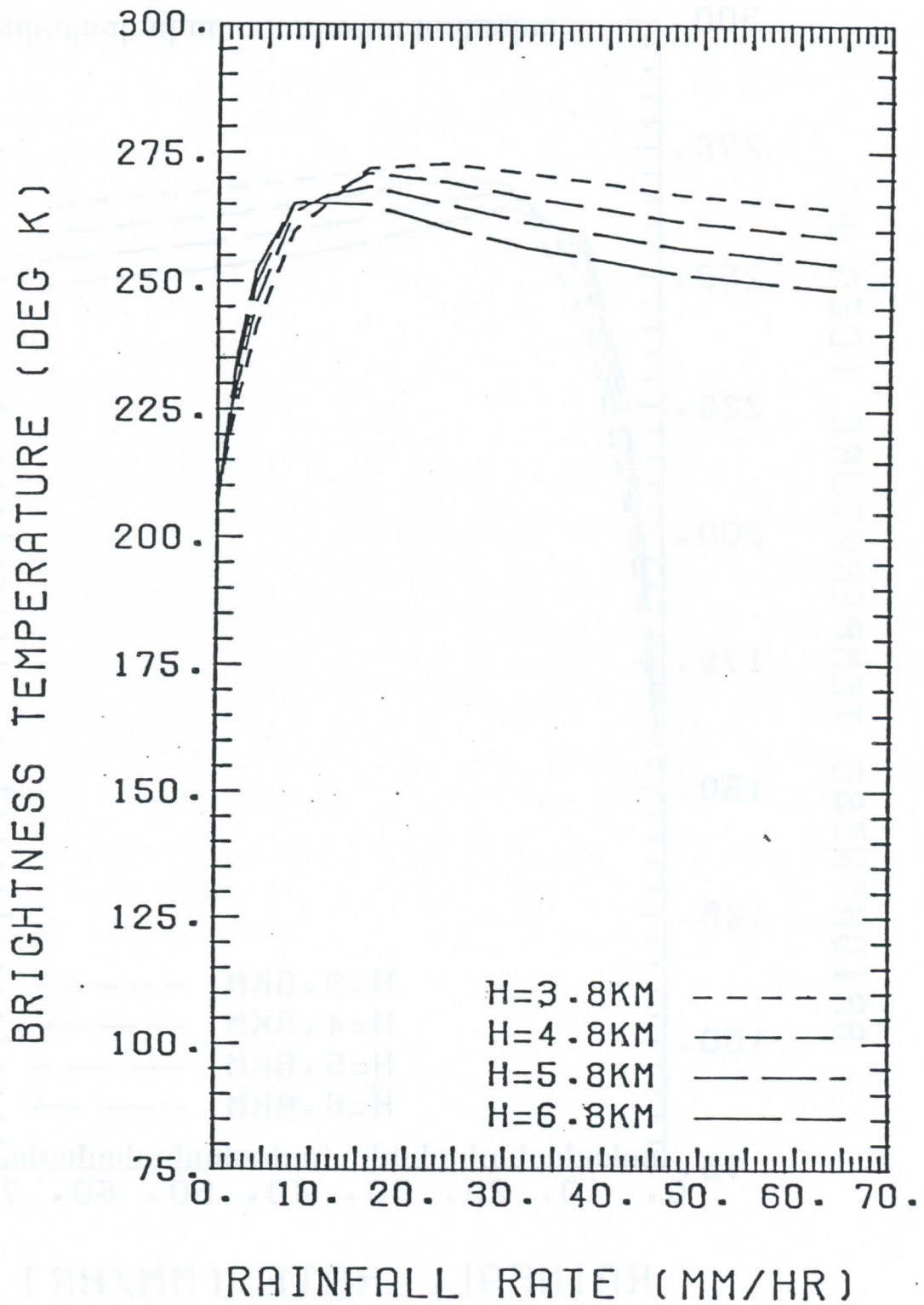Fig. 5.4 10.7 GHz, horizontal polarization.

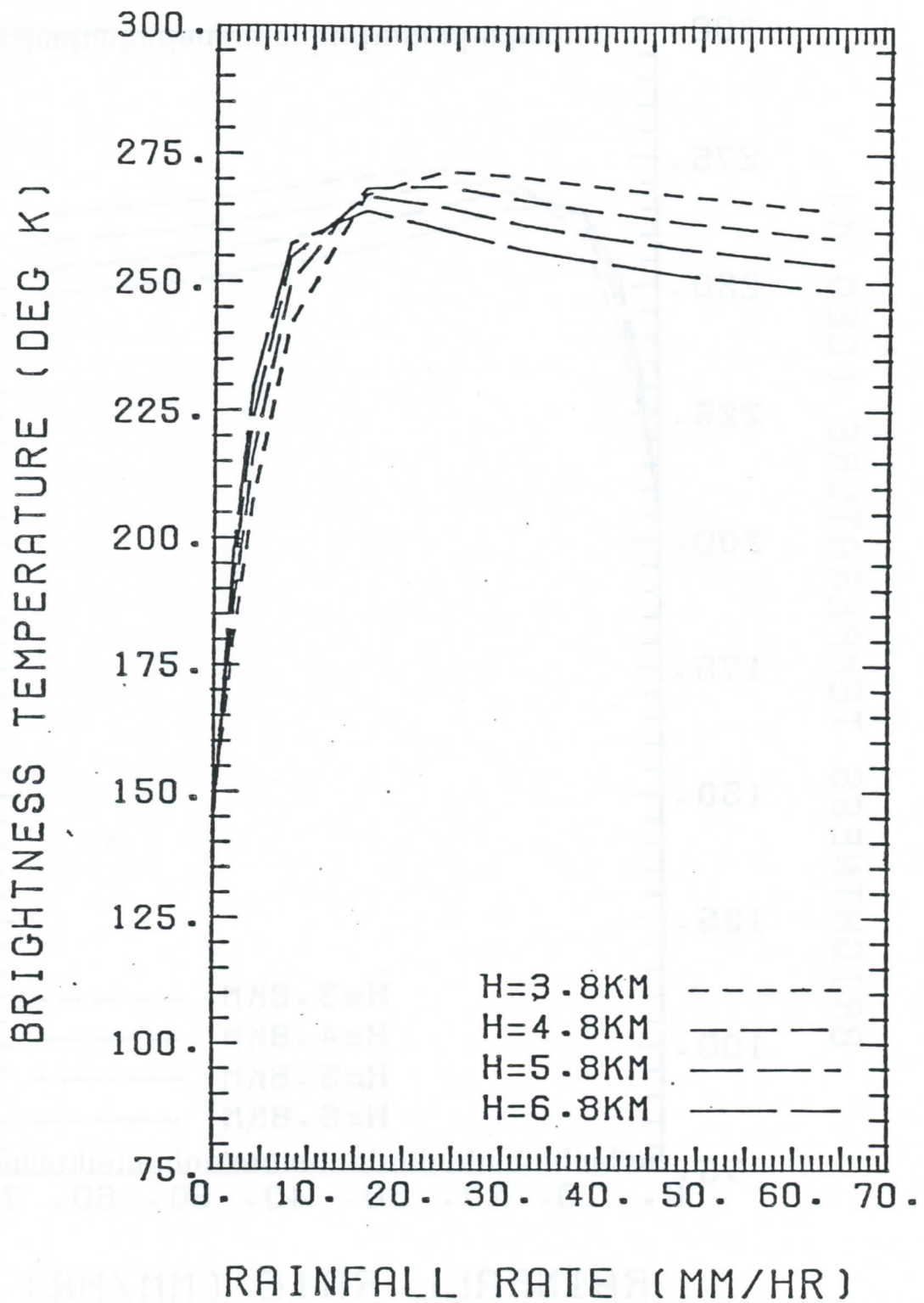Fig. 5.5   18 GHz, vertical polarization.
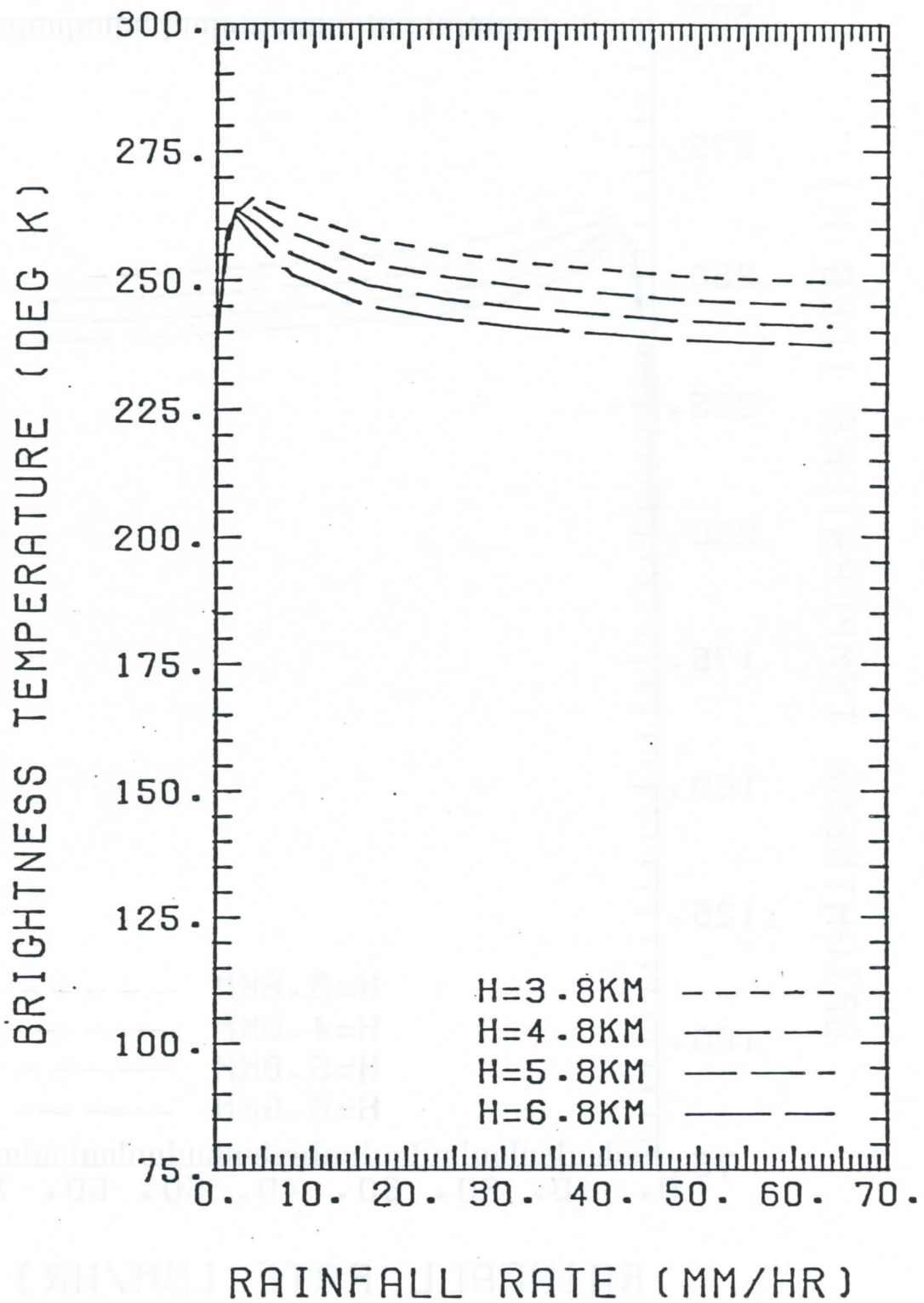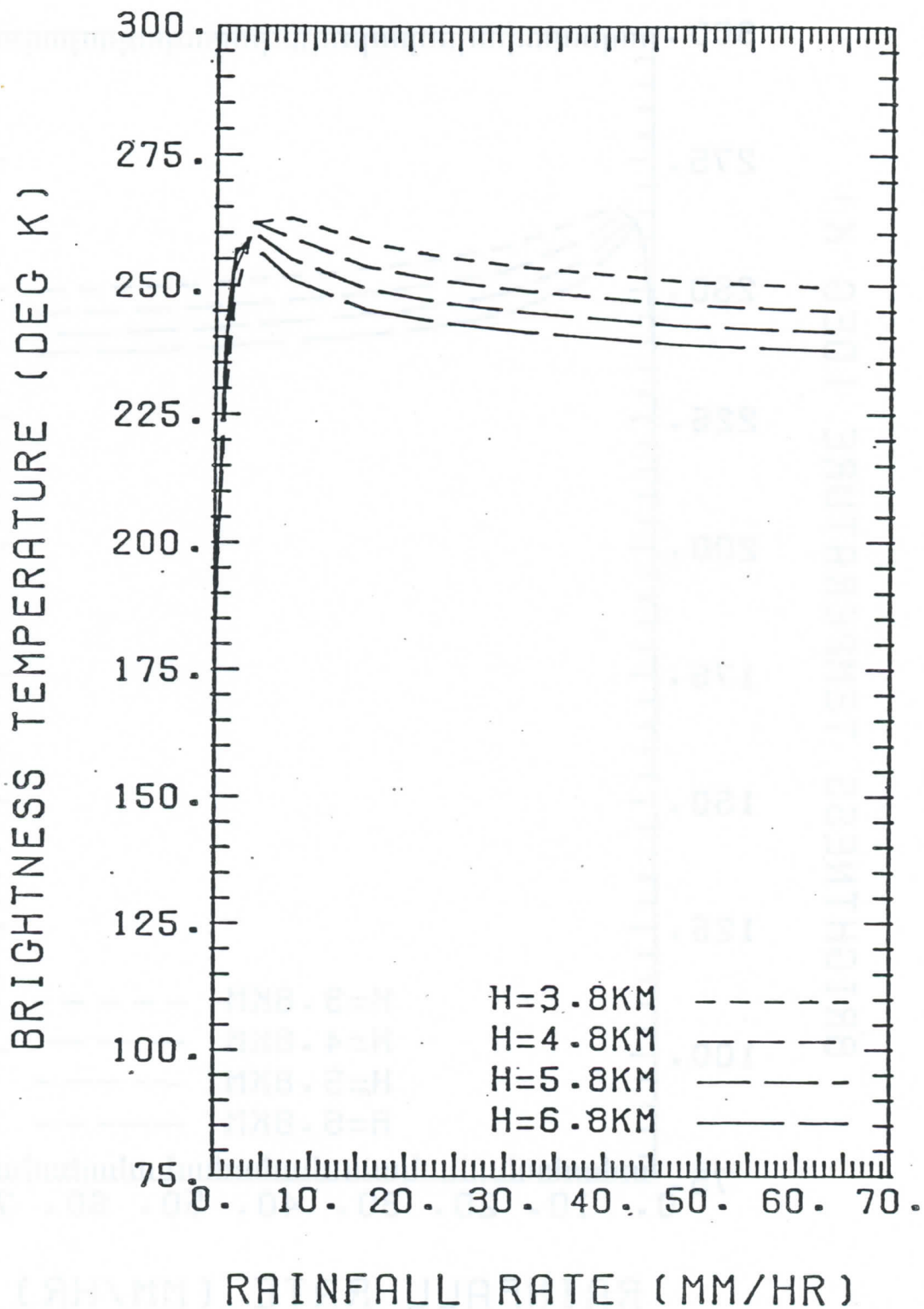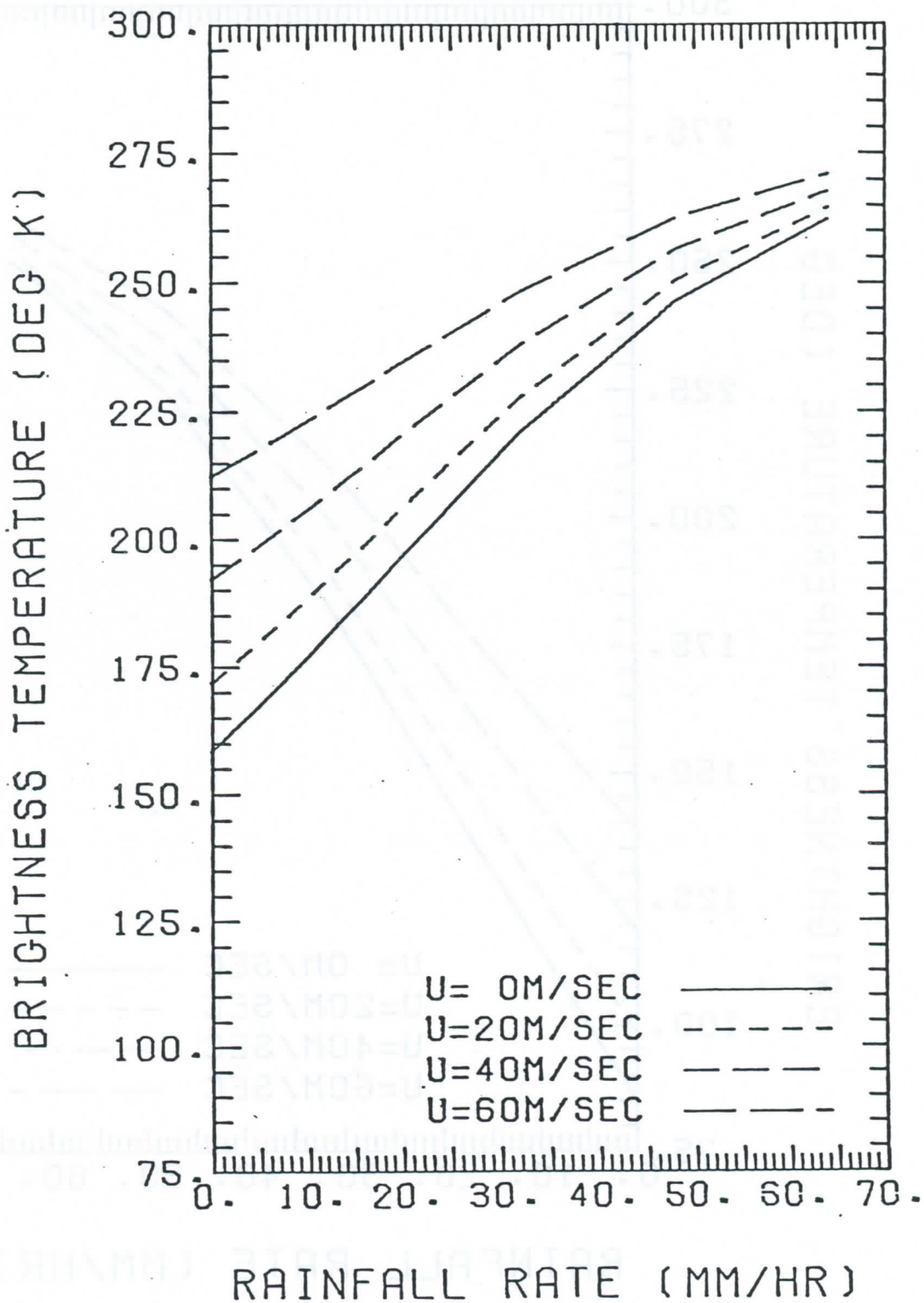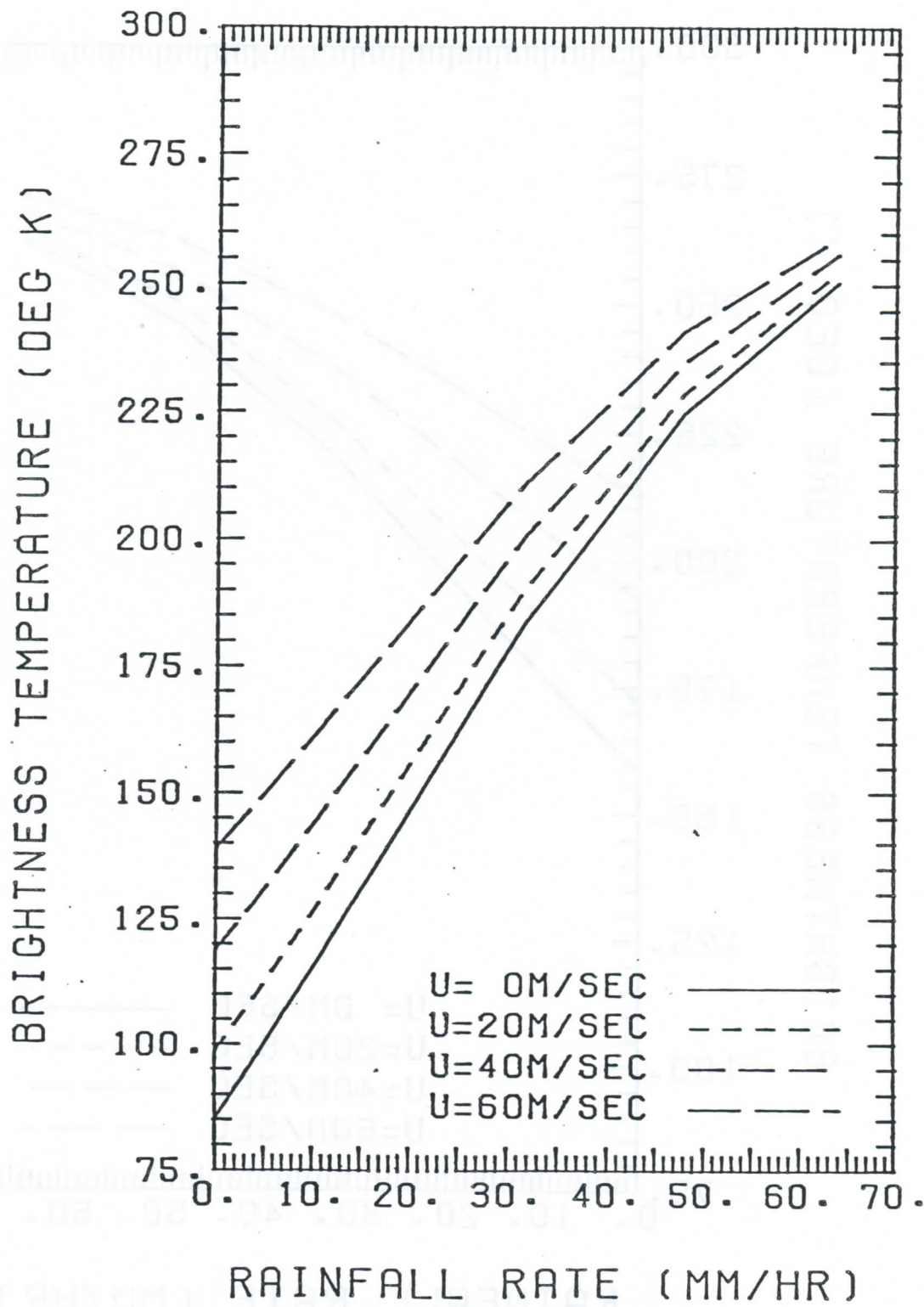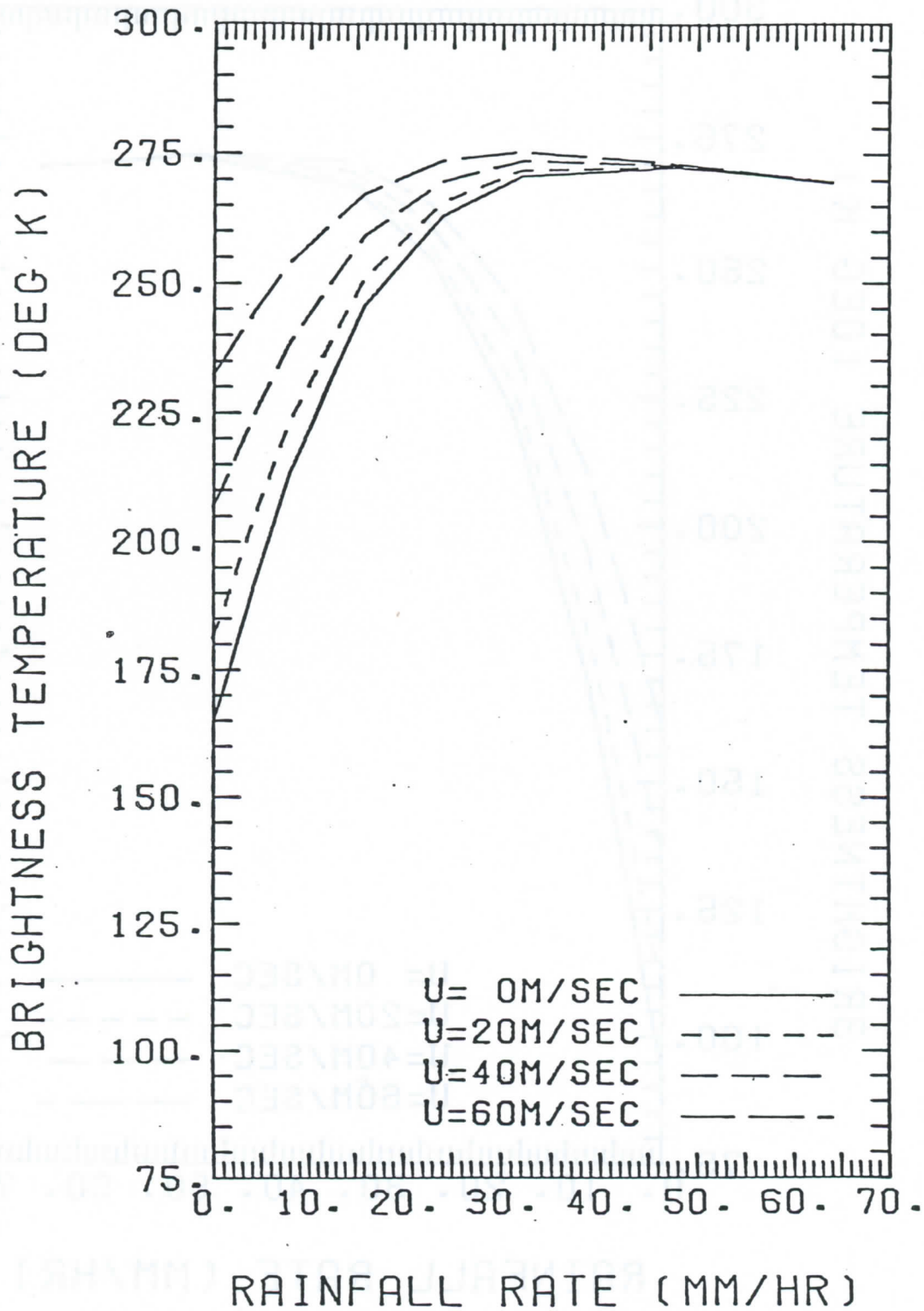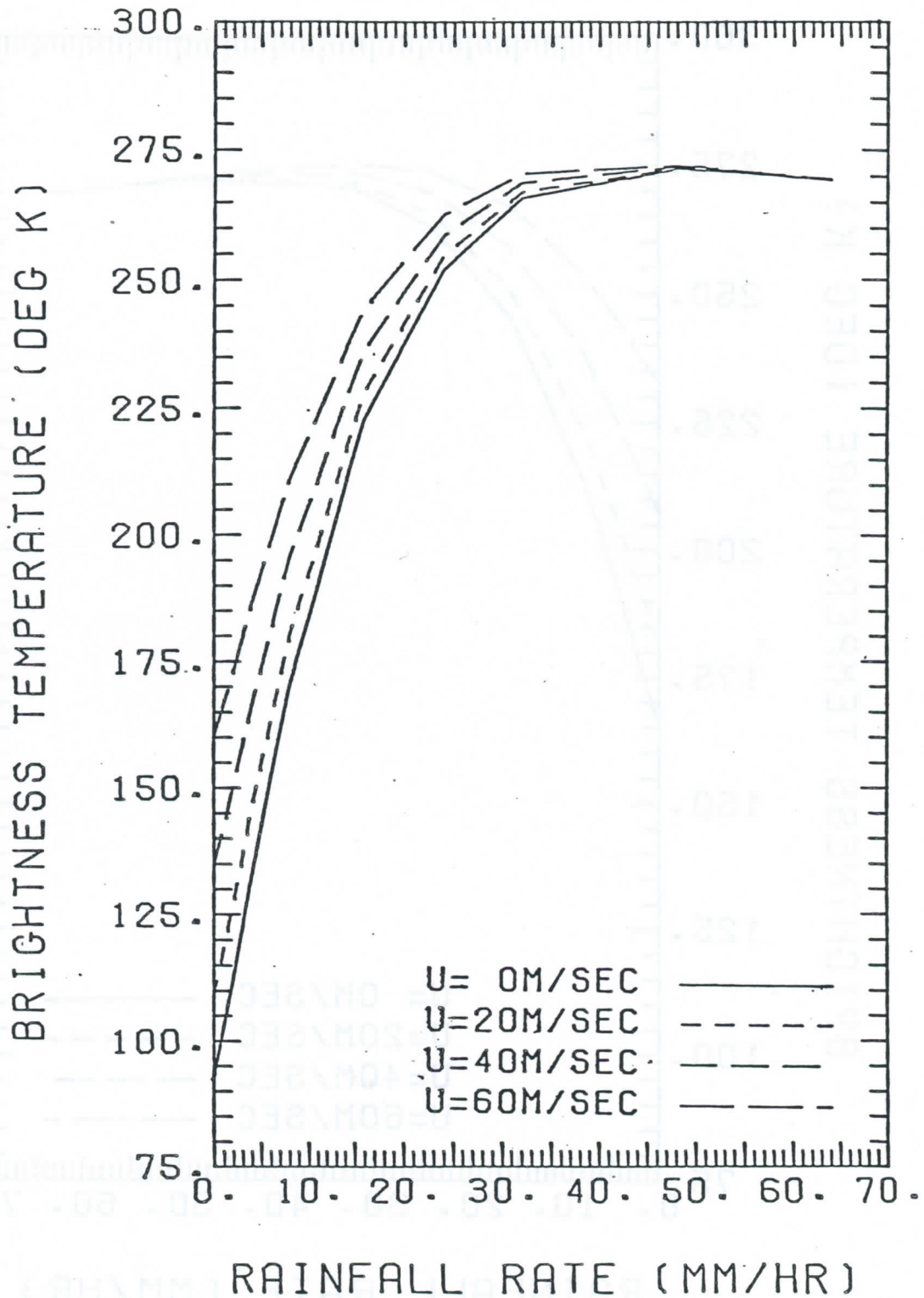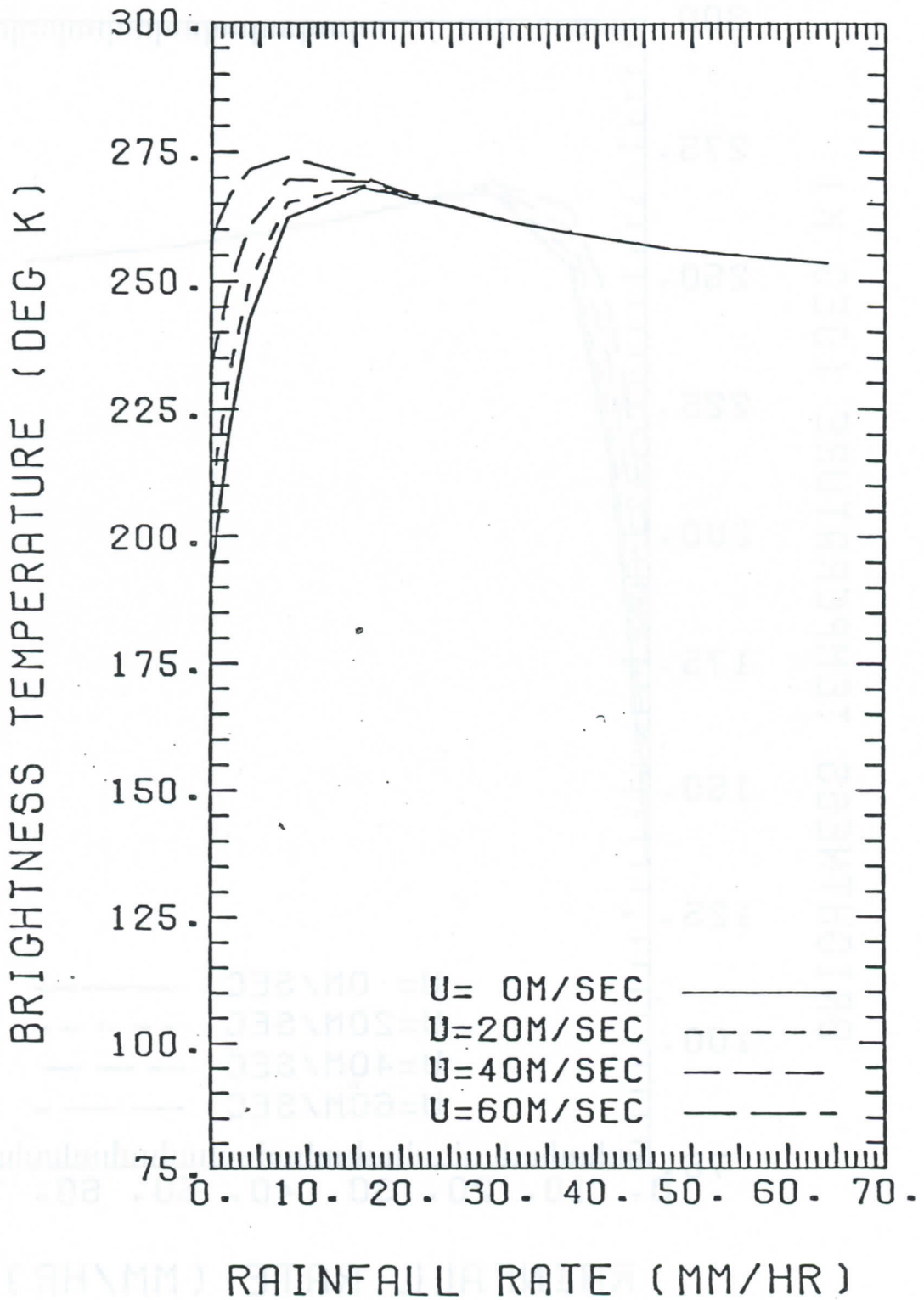
Fig. 5.6 18 GHz, horizontal polarization.

Fig. 5.7   37 GHz, vertical polarization.

Fig. 5.8   37 GHz, horizontal polarization.

Fig. 5.9 6.63 GHz, vertical polarization.

Fig. 5.10   6.63 GHz, horizontal polarization.

Fig. 5.11   10.7 GHz, vertical polarization.

Fig. 5.12   10.7 GHz, horizontal polarization.

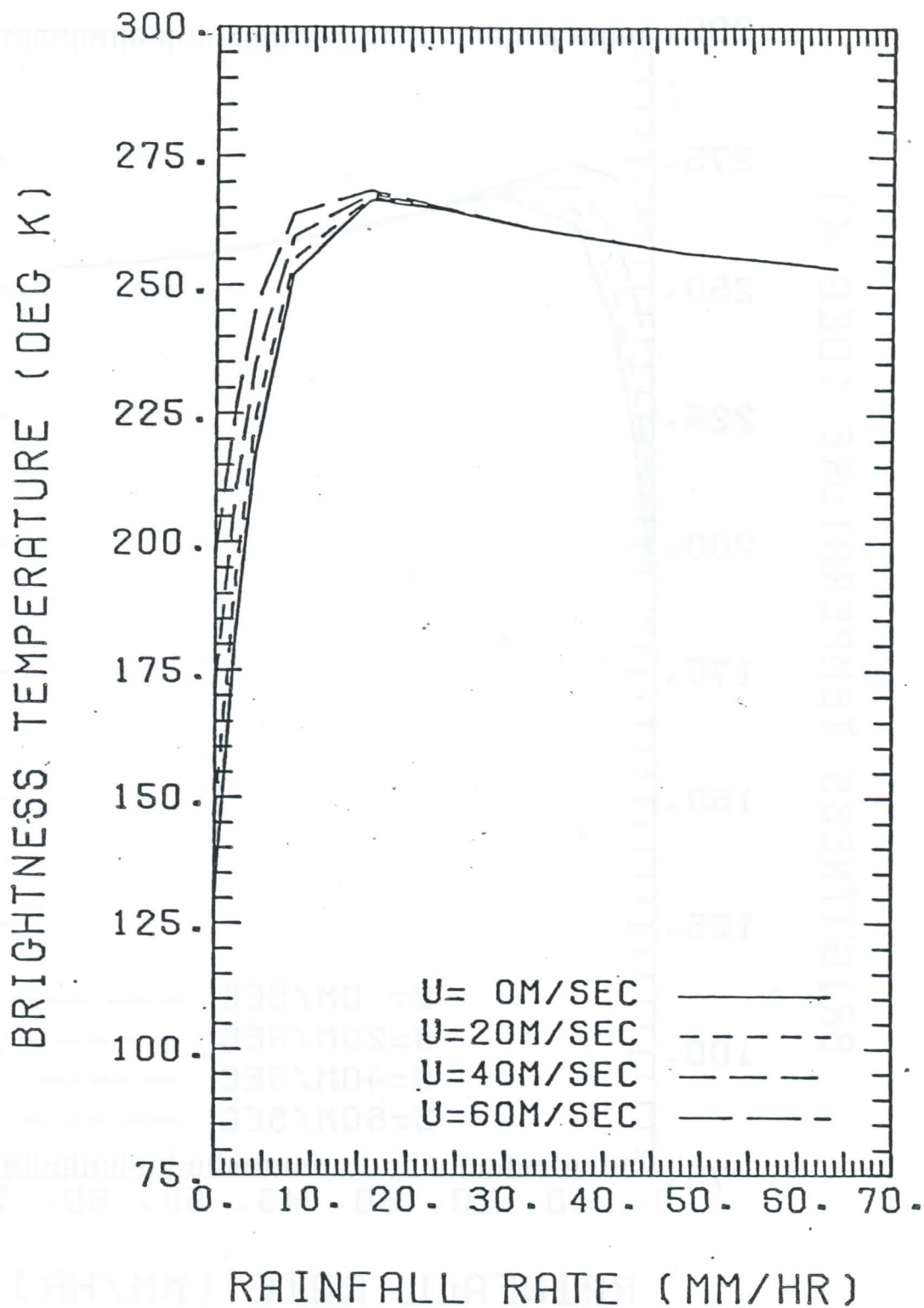Fig. 5.13 18 GHz, vertical polarization.

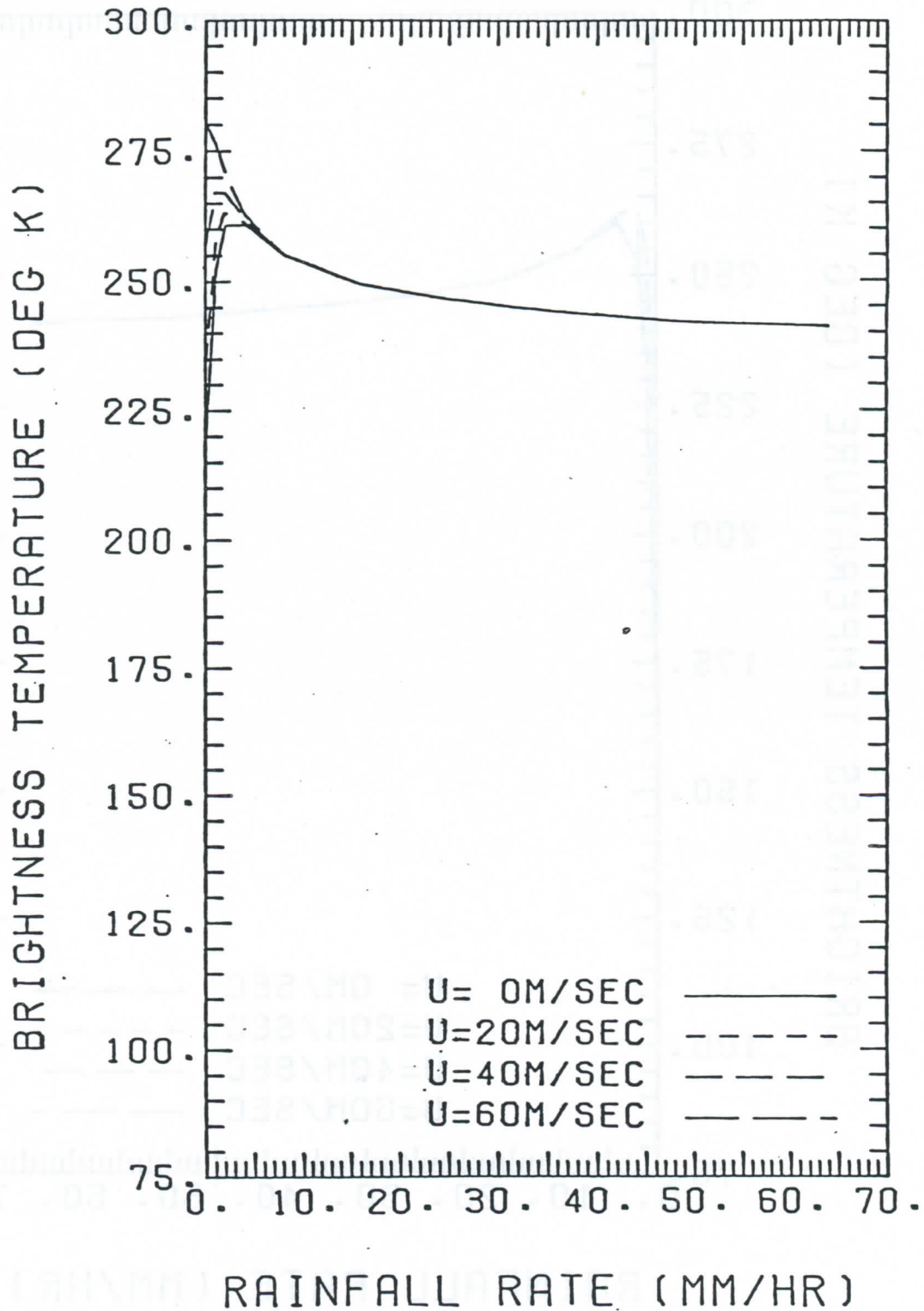Fig. 5.14   18 GHz, horizontal polarization.

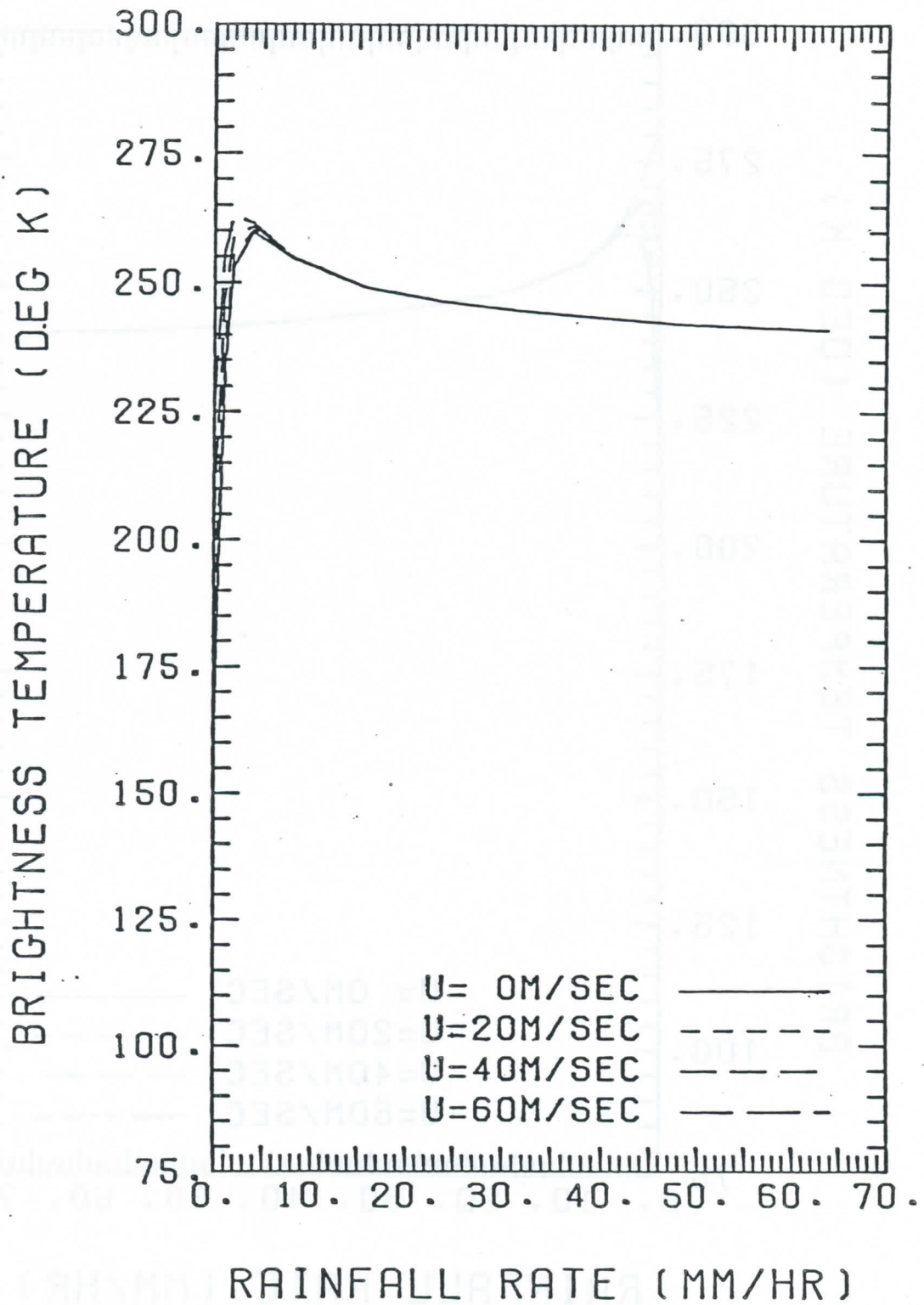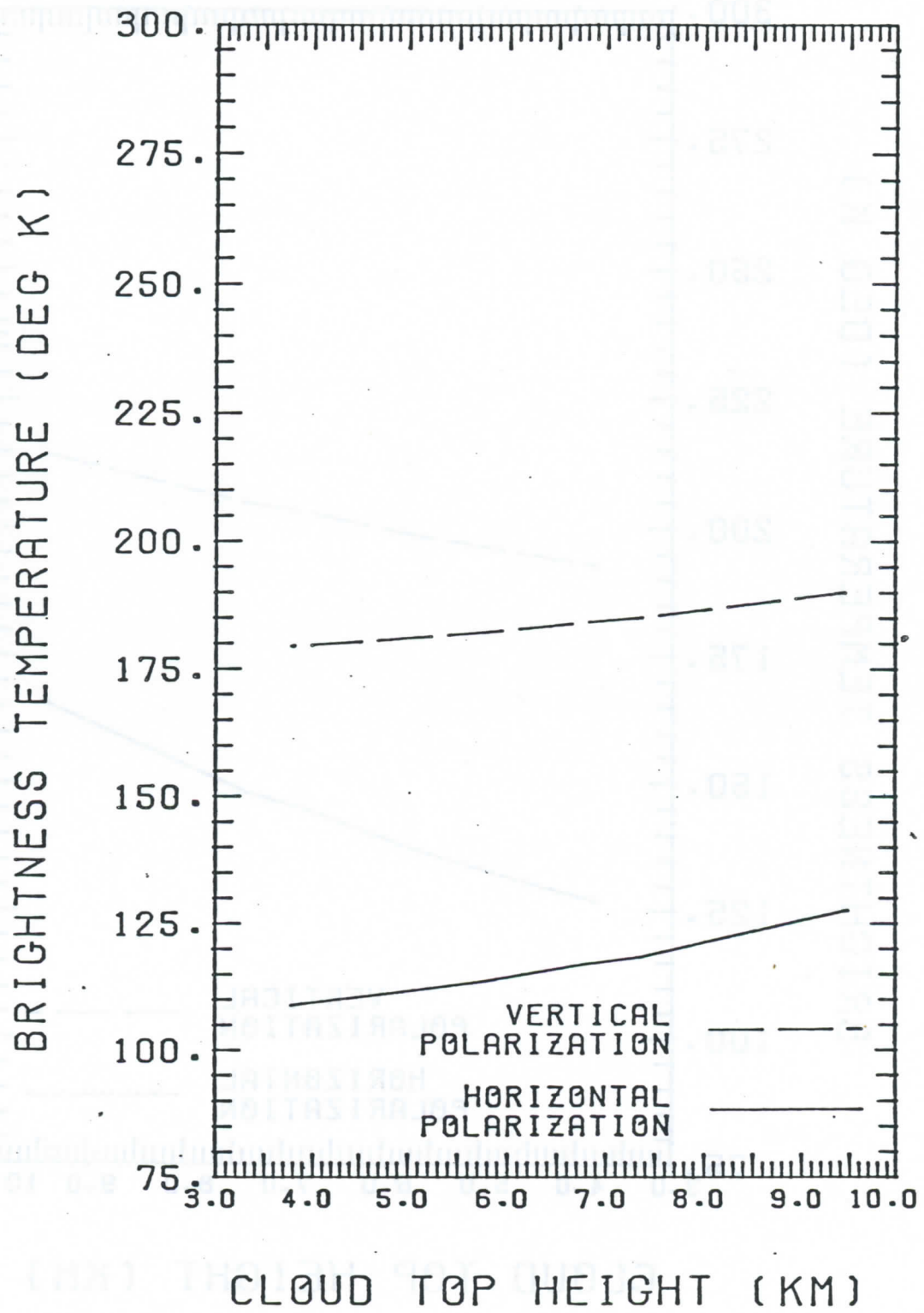Fig. 5.15 37 GHz, vertical polarization.

Fig. 5.16   37 GHz, horizontal polarization.
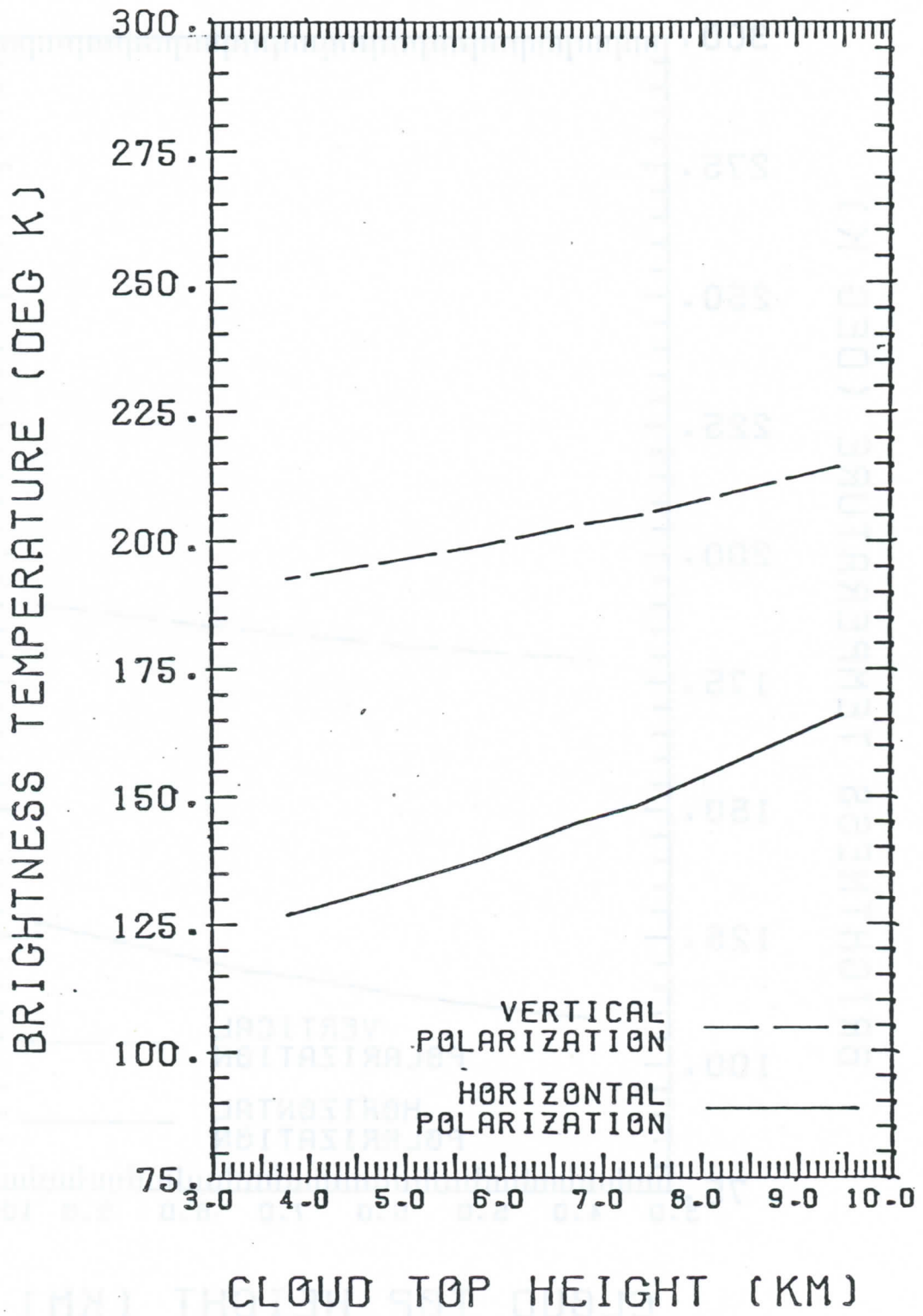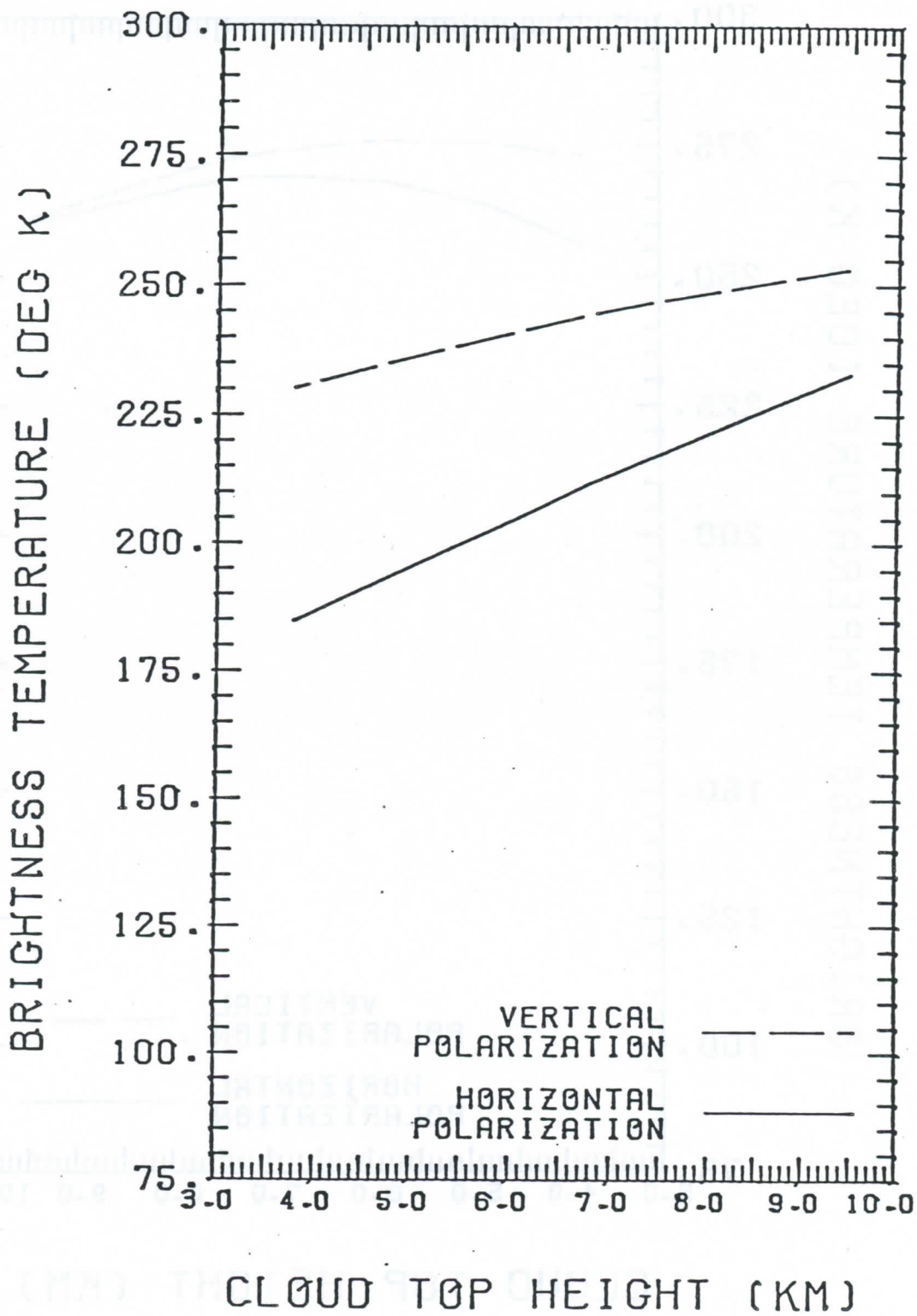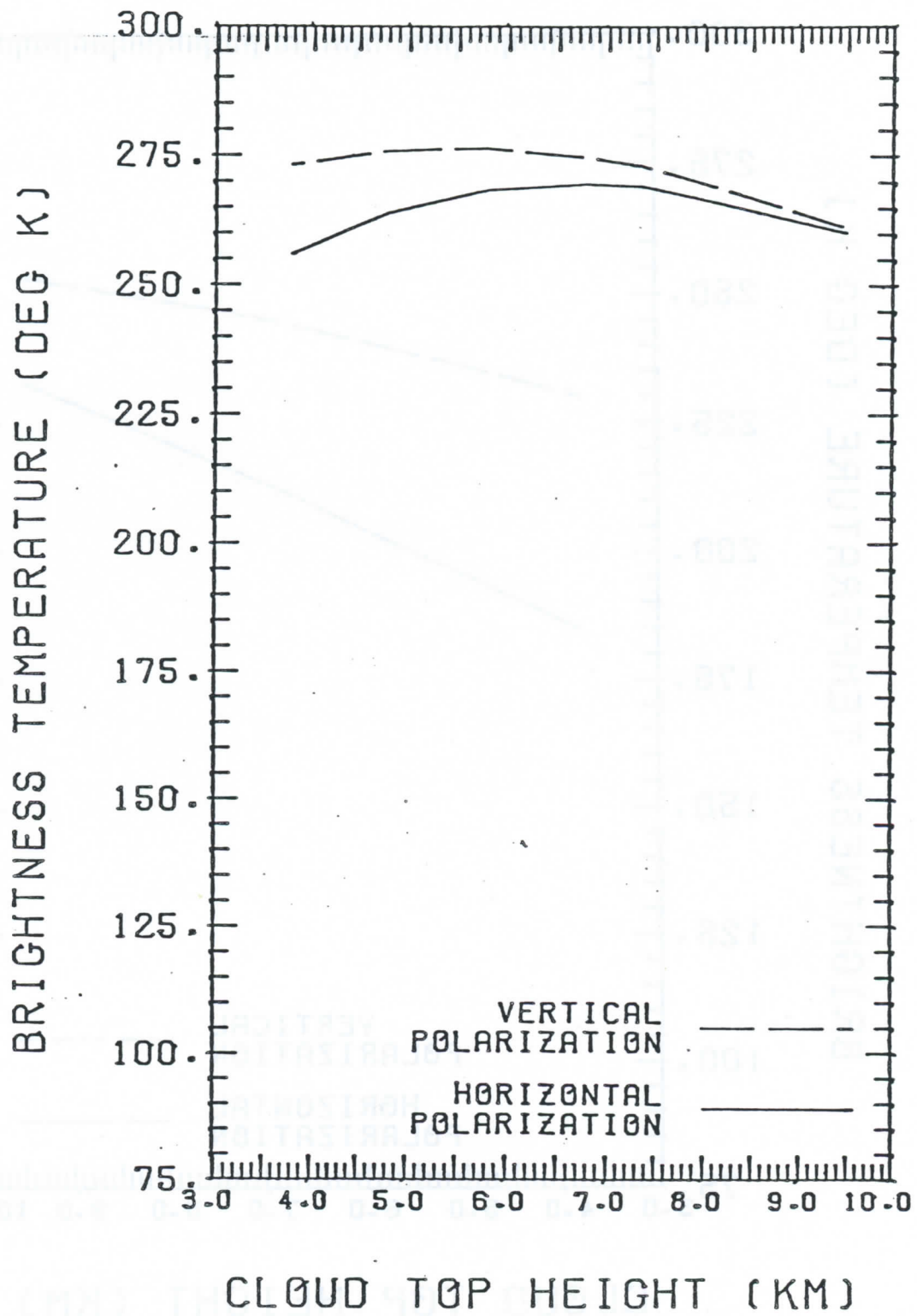
Fig. 5.17 · 6.63 GHz.

Fig. 5.18 10.7 GHz.

Fig. 5.19   18 GHz.

Fig. 5.20   37 GHz.

Table 6.1 Best-fit parameters for the analytical brightness temperature curve fits. The parameters A and α listed yield values of $\tilde{k}_{ext_R}$ in km^{-1} for R in mm/hr (see Eq. 7-3).

6.63 GHz, vertical polarization

(2 mm/hr $\leqslant$ R $\leqslant$ 64 mm/hr)

$$A = 4.00 \times 10^{-4}$$
$$\alpha = 1.29$$
$$T_1 = 3.06 \times 10^{2} {}^{\circ}K$$
$$T_2 = -3.14 {}^{\circ}K/km$$

Root-mean-square deviation = $1.23 {}^{\circ}K$

6.63 GHz, horizontal polarization

(2 mm/hr $\leqslant$ R $\leqslant$ 64 mm/hr)

$$A = 3.89 \times 10^{-4}$$
$$\alpha = 1.29$$
$$T_1 = 3.14 \times 10^{2} {}^{\circ}K$$
$$T_2 = -3.13 {}^{\circ}K/km$$

Root-mean-square deviation = $1.96 {}^{\circ}K$

10.7 GHz, vertical polarization

(2 mm/hr $\leqslant$ R $\leqslant$ 64 mm/hr)

$$A = 2.64 \times 10^{-3}$$
$$\alpha = 1.20$$
$$T_1 = 2.90 \times 10^{2} {}^{\circ}K$$
$$T_2 = -3.29 {}^{\circ}K/km$$

Root-mean-square deviation = $1.37 {}^{\circ}K$

10.7 GHz, horizontal polarization

(2 mm/hr $\leqslant$ R $\leqslant$ 64 mm/hr)

$$A = 2.62 \times 10^{-3}$$
$$\alpha = 1.19$$
$$T_1 = 2.92 \times 10^{2} {}^{\circ}K$$
$$T_2 = -3.49 {}^{\circ}K/km$$

Root-mean-square deviation = $1.64 {}^{\circ}$

Table 6.1 (cont.)

18. GHz, vertical polarization

(2 mm/hr < R < 24 mm/hr)

$$A = 1.35 \times 10^{-2}$$
$$\alpha = 1.08$$
$$T_1 = 2.82 \times 10^{2}{}^{\circ}K$$
$$T_2 = -2.77^{\circ}K/km$$

Root-mean-square deviation = $1.36^{\circ}K$

(24 mm/hr < R < 64 mm/hr)

$$G = 3.10 \times 10^{10}K$$
$$D = 2.73 \times 10^{-2} \, hr/mm$$
$$T_3 = 2.76 \times 10^{2}{}^{\circ}K$$
$$T_4 = -4.87^{\circ}K/km$$

Root-mean-square deviation = $.522^{\circ}K$

18. GHz, horizontal polarization

(2 mm/hr < R < 24 mm/hr)

$$A = 1.27 \times 10^{-2}$$
$$\alpha = 1.08$$
$$T_1 = 2.82 \times 10^{2}{}^{\circ}K$$
$$T_2 = -2.79^{\circ}K/km$$

Root-mean-square deviation = $1.25^{\circ}K$

(24 mm/hr < R < 64 mm/hr)

$$G = 2.96 \times 10^{10}K$$
$$D = 2.26 \times 10^{-2} \, hr/mm$$
$$T_3 = 2.74 \times 10^{2}{}^{\circ}K$$
$$T_4 = -4.76^{\circ}K/km$$

Root-mean-square deviation = $.736^{\circ}K$

Table 6.1 (cont.)

37. GHz, vertical polarization

(1 mm/hr < R < 8 mm/hr)

$A = 8.61 \times 10^{-2}$
$\alpha = 9.05 \times 10^{-1}$
$T_1 = 2.72 \times 10^{20}\,K$
$T_2 = -2.26\,^{o}K/km$

Root-mean-square deviation = $2.67\,^{o}K$

(8 mm/hr < R < 64 mm/hr)

$G = 2.18 \times 10^{10}\,K$
$D = 5.44 \times 10^{-2}\,hr/mm$
$T_3 = 2.65 \times 10^{20}\,K$
$T_4 = -4.18\,^{o}K/km$

Root-mean-square deviation = $.387\,^{o}K$

37. GHz, horizontal polarization

(1 mm/hr < R < 8 mm/hr)

$A = 7.10 \times 10^{-2}$
$\alpha = 1.06$
$T_1 = 2.70 \times 10^{20}\,K$
$T_2 = -2.05\,^{o}K/km$

Root-mean-square deviation = $2.18\,^{o}K$

(8 mm/hr < R < 64 mm/hr)

$G = 2.14 \times 10^{10}\,K$
$D = 5.33 \times 10^{-2}\,hr/mm$
$T_3 = 2.65 \times 10^{20}\,K$
$T_4 = -4.16\,^{o}K/km$

Root-mean-square deviation = $.377\,^{o}K$

Table 7.1 Coefficients for the rainfall rate regression on synthetic brightness temperature data with σ_{noise} = .5°K, 2°K, and 4°K.

$$R = a_o + \sum_{i=1}^{8} a_i \ TB_i$$

where

        TB_1 - 6.63 GHz, vertical channel

        TB_2 - 6.63 GHz, horizontal channel

        TB_3 - 10.7 GHz, vertical channel

        TB_4 - 10.7 GHz, horizontal channel

        TB_5 - 18. GHz, vertical channel

        TB_6 - 18. GHz, horizontal channel

        TB_7 - 37. GHz, vertical channel

        TB_8 - 37. GHz, horizontal channel

Units: R[mm/hr]

        TB_i[°K]

        a_o[mm/hr]

        a_i, i=1,...,8[mm/hr-°K]

Table 7.1 (cont.)

Rainfall Rate Interval

	0-4mm/hr	4-8mm/hr	8-16mm/hr	16-24mm/hr	24-32mm/hr	32-64mm/hr
σ_{noise} = .5°K						
a_0	-21.32	-69.91	-115.9	-166.8	-216.4	-464.7
a_1	-.0998	-.1936	-.1567	-.5454	-.6003	-.2564
a_2	0.000	-.0158	.1394	.5351	.6624	.8013
a_3	.0355	.1120	-.3213	-.3673	-.0124	-.2442
a_4	-.0250	.1552	.3585	.3817	.1757	0.000
a_5	.0509	-.0807	.1590	.1382	-.0553	.2655
a_6	.0512	0.000	0.000	.0750	-.1543	.4248
a_7	.1301	.1452	.2733	.3915	.5758	.3969
a_8	-.0728	.1824	.1233	.2614	.5295	.7798
Explained Variance	.9826	.9695	.9784	.9226	.8934	.9843
σ_{noise} = 2°K						
a_0	-8.318	-45.87	-123.5	-140.9	-193.0	-461.1
a_1	-.0364	-.0842	-.0205	-.1393	-.0699	.3429
a_2	-.0115	-.0236	-.0312	.0916	.2386	.3899
a_3	0.000	.0655	-.0130	.1754	.0736	-.1162
a_4	-.0062	.0720	.1821	.1511	.1525	.1034
a_5	.0243	0.000	.1564	.0865	0.000	.3446
a_6	.0461	.0233	.0539	0.000	0.000	.3734
a_7	.0392	.0526	.1502	.0984	.3500	.2952
a_8	-.0233	.0970	.0621	.1873	.1991	.3506
Explained Variance	.9642	.8342	.9349	.7476	.6902	.9617

Table 7.1 (cont.)

Rainfall Rate Interval

$\sigma_{noise} = 4°K$	0-4mm/hr	4-8mm/hr	8-16mm/hr	16-24mm/hr	24-32mm/hr	32-64mm/hr
a_0	-4.842	-21.72	-95.04	-99.53	-119.9	-376.4
a_1	-.0222	-.0373	.0194	-.0487	.0074	.3158
a_2	0.000	-.0145	-.0143	.0467	.1551	.3533
a_3	-.0125	.0308	.0221	.1724	.0686	-.0355
a_4	0.000	.0509	.1165	.0938	.0818	.1181
a_5	.0191	.0075	.1072	.0684	-.0108	.2762
a_6	.0392	.0264	.0776	-.0062	.0124	.2666
a_7	.0106	.0098	.0763	.0388	.1988	.2225
a_8	-.0056	.0410	.0329	.1184	.1224	.2159
Explained Variance	.9467	.7240	.8875	.6465	.5376	.9110

Table 7.2 Coefficients for the precipitation column height
regression on synthetic brightness temperature data with
σ_{noise} = .5°K, 2°K, and 4°K.

$$H = b_o + \sum_{i=1}^{8} b_i \ TB_i$$

where

       TB_1 - 6.63 GHz, vertical channel

       TB_2 - 6.63 GHz, horizontal channel

       T_{B3} - 10.7 GHz, vertical channel

       TB_4 - 10.7 GHz, horizontal channel

       TB_5 - 18. GHz, vertical channel

       TB_6 - 18. GHz, horizontal channel

       TB_7 - 37. GHz, vertical channel

       TB_8 - 37. GHz, horizontal channel

Units: H[km]

       TB_i[°K]

       b_o[km]

       b_i, i=1,...,8 [km/°K]

Table 7.2 (cont.)

Rainfall Rate Interval

	0-4mm/hr	4-8mm/hr	8-16mm/hr	16-24mm/hr	24-32mm/hr	32-64mm/hr
$\sigma_{noise} = .5^{\circ}K$						
b_0	131.9	95.45	88.54	83.88	77.62	80.02
b_1	-.1457	.1325	-.0231	.0535	.0446	.0043
b_2	.1437	0.000	.0346	-.0596	-.0480	-.0221
b_3	-.2298	-.1296	.0502	.0228	-.0060	-.0022
b_4	.4395	-.0626	-.0684	-.0122	-.0041	-.0160
b_5	-.1171	.0518	-.0795	-.0897	-.0217	-.0604
b_6	-.1634	.0600	.0308	-.0229	0.000	-.0741
b_7	-.5357	-.1658	-.1543	-.0998	-.1286	-.0559
b_8	.2816	-.2369	-.1138	-.1131	-.1350	-.0714
Explained Variance	.6095	.9692	.9860	.9872	.9941	.9911
$\sigma_{noise} = 2^{\circ}K$						
b_0	39.16	64.71	80.66	71.10	61.75	73.56
b_1	-.0218	.0467	-.0443	.0052	.0068	-.0182
b_2	.0464	-.0054	.0520	0.000	-.0100	-.0031
b_3	-.0696	-.0769	0.000	-.0396	-.0072	-.0196
b_4	.0725	0.000	-.0226	.0180	0.000	-.0207
b_5	.0210	.0104	-.0854	-.0699	-.0257	-.0518
b_6	-.0355	.0325	0.000	-.0387	-.0084	-.0619
b_7	-.1732	-.0943	-.1020	-.0464	-.0871	-.0510
b_8	.0659	-.1427	-.0798	-.0814	-.0955	-.0416
Explained Variance	.2613	.7428	.8945	.9175	.9605	.9260

Table 7.2 (cont.)

Rainfall Rate Interval

$\sigma_{noise} = 4°K$	0-4mm/hr	4-8mm/hr	8-16mm/hr	16-24mm/hr	24-32mm/hr	32-64mm/hr
b_0	15.35	27.27	59.58	47.40	41.05	57.78
b_1	0.000	.0202	−.0406	.0065	.0058	−.0138
b_2	.0107	−.0088	.0361	.0078	.0022	−.0020
b_3	−.0263	−.0325	0.000	−.0319	−.0038	−.0202
b_4	.0349	.0081	−.0050	.0231	.0088	−.0137
b_5	.0258	.0071	−.0637	−.0466	−.0200	−.0418
b_6	−.0168	.0305	−.0127	−.0338	−.0041	−.0479
b_7	−.0621	−.0467	−.0634	−.0245	−.0583	−.0379
b_8	.0124	−.0618	−.0540	−.0576	−.0717	−.0282
Explained Variance	.1698	.5436	.7474	.8021	.9155	.7902

Table 7.3 Coefficients for the 20-meter wind speed regression on synthetic brightness temperature data with σnoise = .5°K, 2°K, and 4°K.

$$U_{20} = c_o + \sum_{i=1}^{8} c_i \, TB_i$$

where

TB_1 — 6.63 GHz, vertical channel

TB_2 — 6.63 GHz, horizontal channel

TB_3 — 10.7 GHz, vertical channel

TB_4 — 10.7 GHz, horizontal channel

TB_5 — 18. GHz, vertical channel

TB_6 — 18. GHz, horizontal channel

TB_7 — 37. GHz, vertical channel

TB_8 — 37. GHz, horizontal channel

Units: U_{20}[m/sec]

TB_i[$^\circ$K]

c_o[m/sec]

c_i, i=1,...,8[m/sec-$^\circ$K]

Table 7.3 (cont.)

Rainfall Rate Interval

	0–4mm/hr	4–8mm/hr	8–16mm/hr	16–24mm/hr	24–32mm/hr	32–64mm/hr
$\sigma_{noise} = .5^\circ K$						
c_0	−99.16	−147.6	−177.8	−276.2	−339.0	−206.3
c_1	.3747	.8453	1.520	1.954	2.340	2.686
c_2	.2741	.5325	−.2601	−.6277	−.9070	−1.620
c_3	.3497	0.000	.4162	.8493	0.000	−.5566
c_4	.1578	−.3851	−.6520	−1.016	−.5282	.2669
c_5	0.000	0.000	−.2487	.1780	.3407	−.1102
c_6	−.2760	.0739	.2843	.5629	.9156	.3316
c_7	−.1583	0.000	−.1270	−.3192	−.8922	.7718
c_8	.1306	0.000	0.000	−.4090	.1217	−1.002
Explained Variance	.9942	.9893	.9709	.9434	.8475	.4771
$\sigma_{noise} = 2^\circ K$						
c_0	−100.0	−129.8	−79.82	−208.7	−110.6	−81.25
c_1	.2675	.5741	.9696	.8431	.6942	.2988
c_2	.2085	.4865	0.000	.2446	.0242	−.1744
c_3	.3776	.1062	.2638	−.1075	.0674	−.0604
c_4	.2067	−.1769	−.3849	−.4721	−.5103	.1425
c_5	0.000	−.0425	−.2446	.0786	−.1075	0.000
c_6	−.2562	−.0950	−.1576	.5985	.1584	.0838
c_7	−.0529	.1214	.0534	.0597	−.3647	.2650
c_8	.0644	0.000	.0913	−.1480	.6593	−.1898
Explained Variance	.9266	.8973	.8111	.7390	.5093	.1132

Table 7.3 (cont.)

Rainfall Rate Interval

| $\sigma_{noise} = 4^{\circ}K$	0-4mm/hr	4-8mm/hr	8-16mm/hr	16-24mm/hr	24-32mm/hr	32-64mm/hr
c_0	-71.18	-79.61	-38.82	-97.51	-9.604	-54.62
c_1	.1638	.3851	.6310	.4221	.2955	.0841
c_2	.1880	.3996	.0156	.2535	.0596	-.0455
c_3	.3039	.0916	.1850	-.1340	.0660	0.000
c_4	.1869	-.0908	-.2182	-.2377	-.2847	.1013
c_5	0.000	-.0383	-.1834	-.0571	-.1505	.0193
c_6	-.1786	-.1007	-.2293	.4598	0.000	.0454
c_7	-.0498	.1210	.1059	.0174	-.2138	.1424
c_8	.0313	-.0666	.0701	-.1158	.4069	-.0792
Explained Variance	.7669	.7315	.5938	.5999	.3772	.0781

Table 7.4 Root-mean-square errors in the geophysical parameter estimates based on the inversion test brightness temperature data where R > .1 mm/hr.

Noise in Regression/Inversion Data	Parameter Mean Values			Root-Mean-Square Error in the Estimate of		
	$\bar{R}$[mm/hr]	$\bar{H}$[km]	$\bar{U}_{20}$[m/sec]	R[mm/hr]	H[km]	U_{20}[m/sec]
σ_{noise} = .5°K	10.6	5.20	16.1	.548	.715	1.46
σ_{noise} = 2°K	10.6	5.20	16.1	1.25	.693	3.04
σ_{noise} = 4°K	10.6	5.20	16.1	1.69	.782	3.60
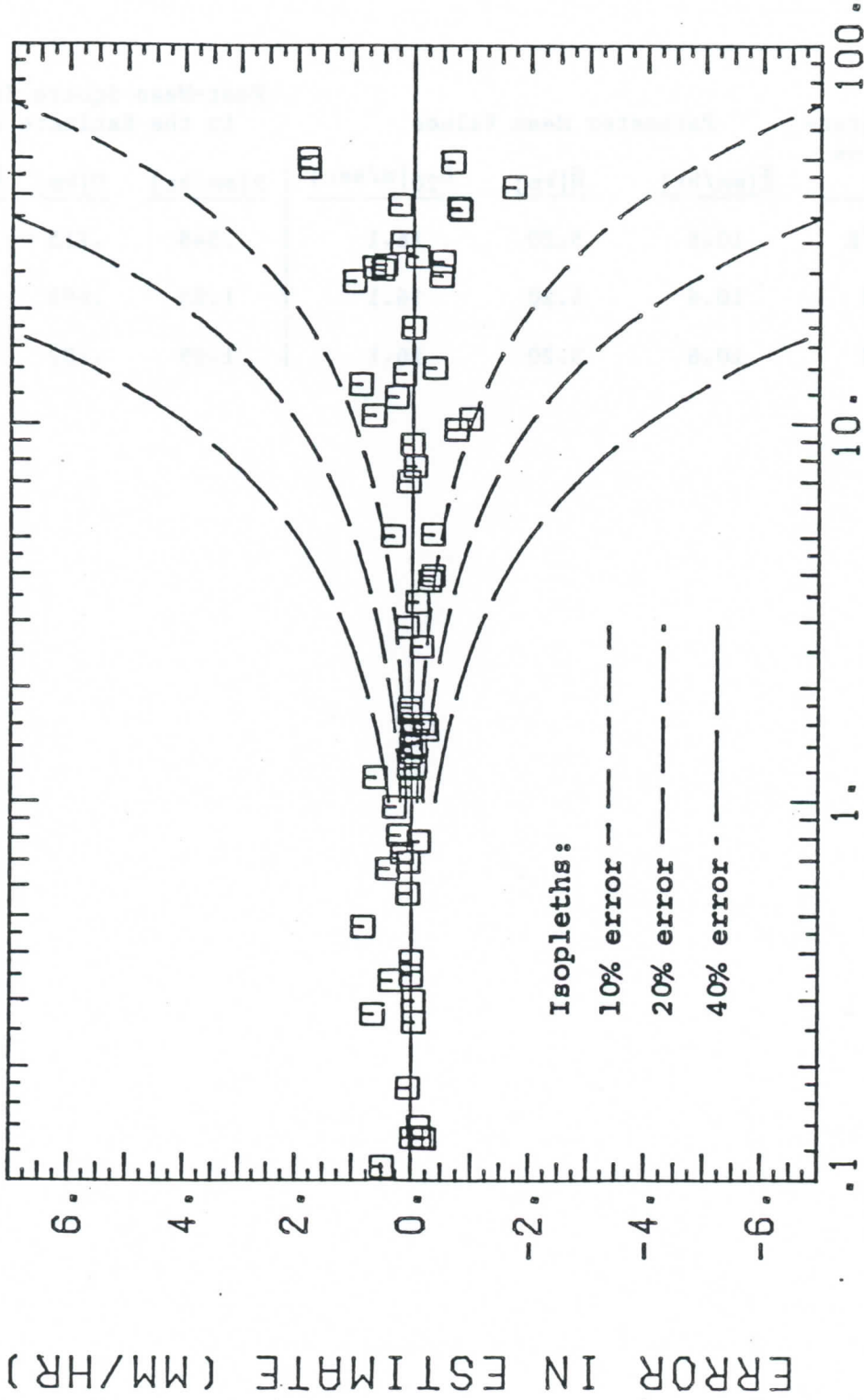
Fig. 7.1 Errors in the inversion estimates of rainfall rate for σ_{noise} = .5°K in the regression/inversion data sets.

RAINFALL RATE (MM/HR)

ERROR IN ESTIMATE (MM/HR)

Isopleths:
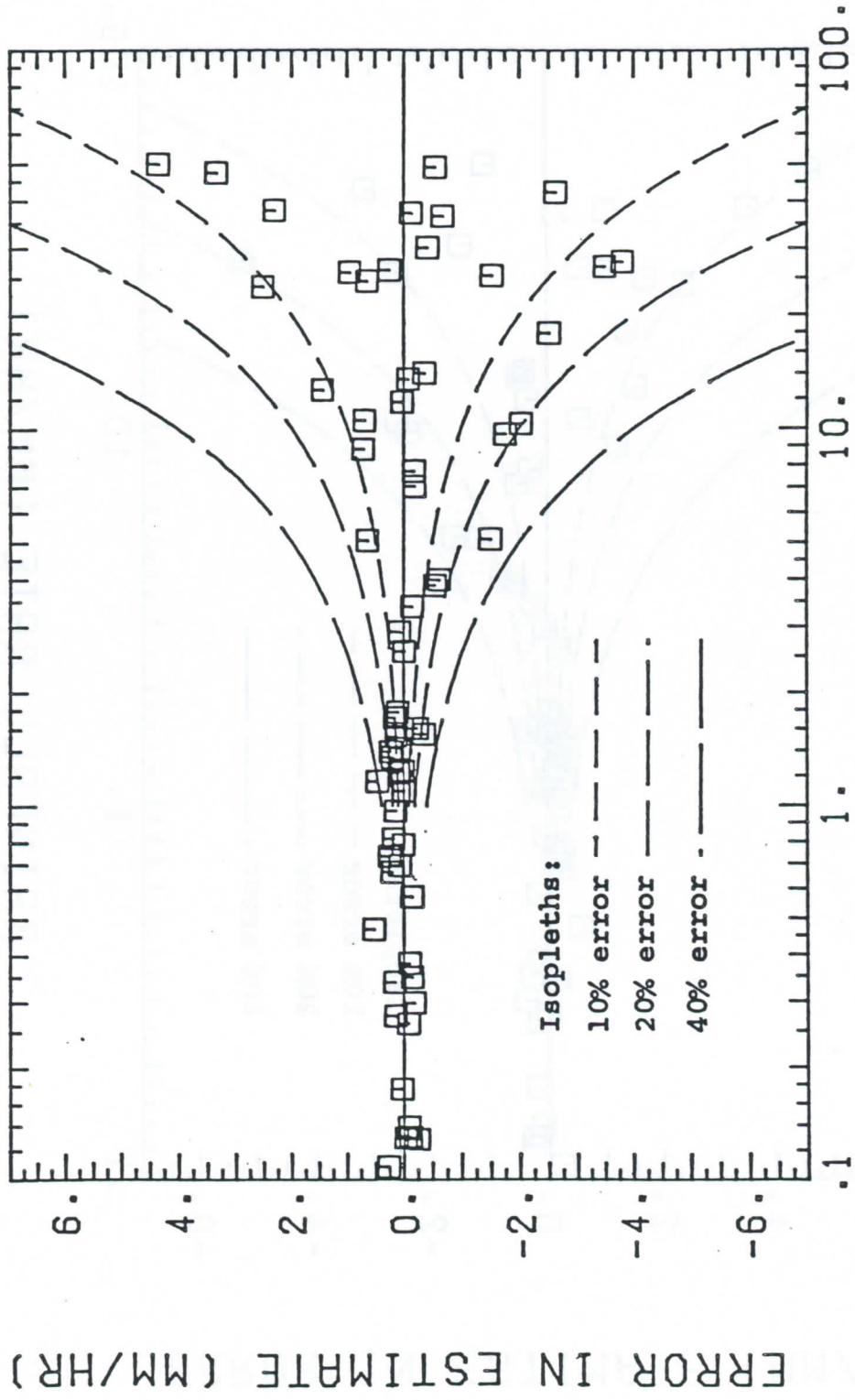
10% error — — —
20% error — — · —
40% error — · — ·

Fig. 7.2 Errors in the inversion estimates of rainfall rate for
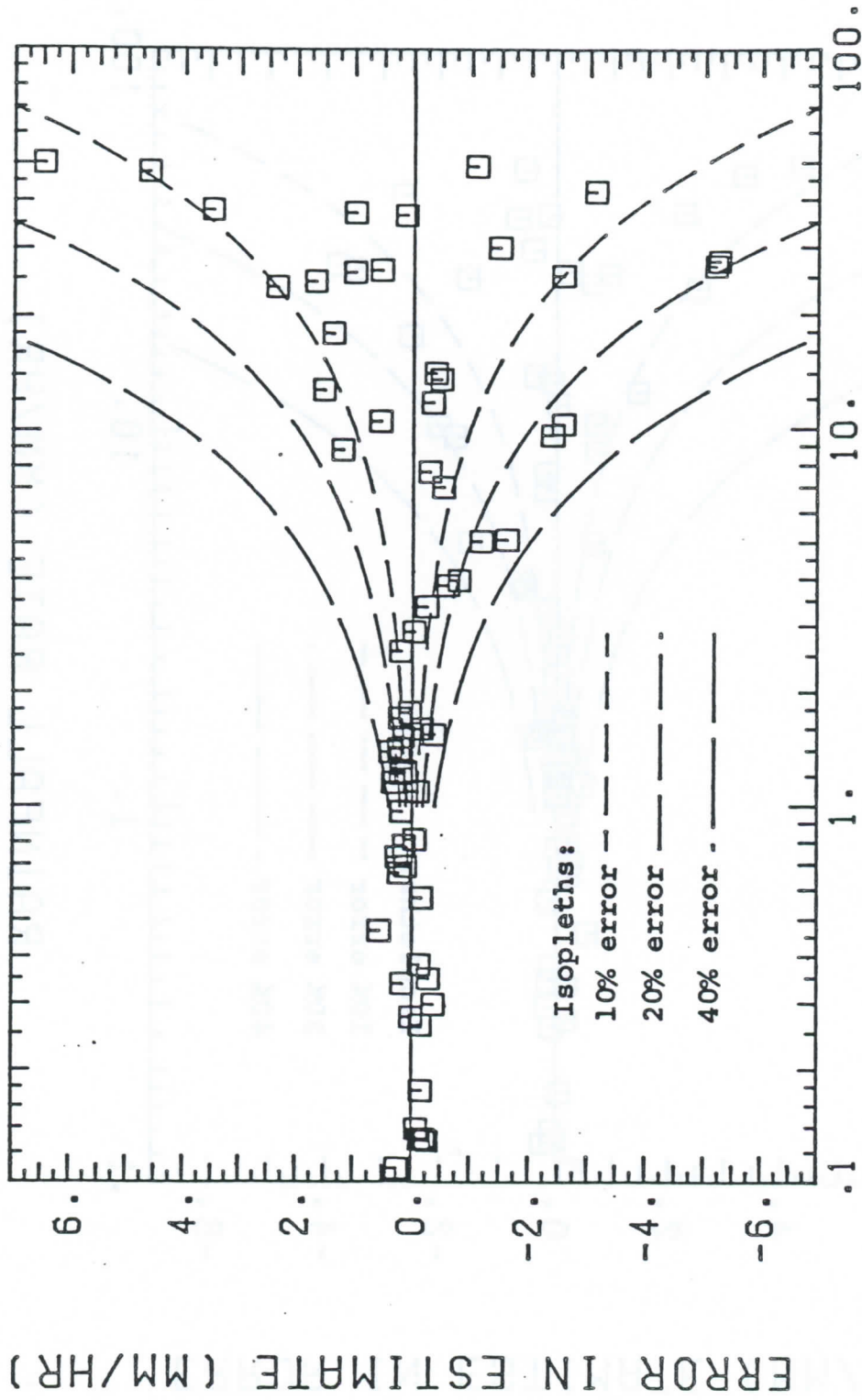$\sigma_{noise} = 2^{\circ}K$ in the regression/inversion data sets.

RAINFALL RATE (MM/HR)

ERROR IN ESTIMATE (MM/HR)

Isopleths:
10% error ----
20% error ——
40% error -·-

Fig. 7.3 Errors in the inversion estimates of rainfall rate for
$\sigma_{noise} = 4^{o}$K in the regression/inversion data sets.

Table 7.5 Coefficients for the rainfall rate, precipitation column height, and 20-meter wind speed regressions on synthetic brightness temperature data with $\sigma_{noise} = 2°K$. A uniform .5 gm/m^3 LWC cloud droplet layer of thickness H is added to the model atmosphere.

$$R = a_o + \sum_{i=1}^{8} a_i \, TB_i$$

$$H = b_o + \sum_{i=1}^{8} b_i \, TB_i$$

$$U_{20} = c_o + \sum_{i=1}^{8} c_i \, TB_i$$

where

TB_1 – 6.63 GHz, vertical channel

TB_2 – 6.63 GHz, horizontal channel

TB_3 – 10.7 GHz, vertical channel

TB_4 – 10.7 GHz, horizontal channel

TB_5 – 18. GHz, vertical channel

TB_6 – 18. GHz, horizontal channel

TB_7 – 37. GHz, vertical channel

TB_8 – 37. GHz, horizontal channel

Units: $R[mm/hr]$, $H[km]$, $U_{20}[m/sec]$

$T_B[°K]$

$a_o[mm/hr]$, $b_o[km]$, $c_o[m/sec]$

a_i, $i=1,\ldots,8[mm/hr-°K]$

b_i, $i=1,\ldots,8[km/°K]$

c_i, $i=1,\ldots,8[m/sec-°K]$

Table 7.5 (cont.)

Rainfall Rate Interval

	0–4mm/hr	4–8mm/hr	8–16mm/hr	16–24mm/hr	24–32mm/hr	32–64mm/hr
R Regression						
a_0	−38.90	−53.74	−151.5	−147.5	−206.4	−499.3
a_1	0.000	−.0886	−.0201	−.1436	−.0626	.3786
a_2	−.0464	−.0414	−.0418	.1011	.2494	.4105
a_3	.0231	.0905	.0151	.2072	.0855	−.1210
a_4	−.0285	.0683	.2066	.1522	.1499	.1156
a_5	.0362	.0251	.1910	.0927	0.000	.3666
a_6	.0695	.0274	.0835	0.000	0.000	.3922
a_7	.0903	.0448	.1524	.0870	.3663	.3175
a_8	−.0079	.0935	.0545	.1766	.2048	.3671
Explained Variance	.9305	.7659	.9196	.7088	.6513	.9572
H Regression						
b_0	80.14	59.45	82.11	70.41	60.90	74.65
b_1	−.0771	.0336	−.0424	.0083	.0068	−.0192
b_2	.0871	.0102	.0553	0.000	−.0082	−.0036
b_3	−.0783	−.0801	−.0078	−.0426	−.0090	−.0214
b_4	.0975	.0326	−.0234	.0172	0.000	−.0225
b_5	−.0172	−.0141	−.0897	−.0689	−.0241	−.0512
b_6	−.0187	.0218	−.0130	−.0418	−.0066	−.0615
b_7	−.1994	−.0764	−.0944	−.0425	−.0868	−.0517
b_8	−.0338	−.1222	−.0702	−.0789	−.0950	−.0409
Explained Variance	.6614	.7525	.8995	.9206	.9599	.9248

Table 7.5 (cont.)

Rainfall Rate Interval

	0-4mm/hr	4-8mm/hr	8-16mm/hr	16-24mm/hr	24-32mm/hr	32-64mm/hr
U_{20} Regression						
c_0	-233.2	-200.1	-118.4	-273.3	-140.4	-81.83
c_1	.4414	.5671	1.064	.8566	.6909	.2848
c_2	.1558	.5221	-.0604	.2342	.0399	-.1642
c_3	.4383	.1802	.2520	-.1130	.0470	-.0581
c_4	.0573	-.2634	-.3907	-.4644	-.5180	.1507
c_5	0.000	-.0486	-.2405	.1060	-.0896	0.000
c_6	-.2810	-.1169	-.2335	.6671	.1675	.0819
c_7	.2092	.2285	.1622	.1126	-.3326	.2628
c_8	.2496	.1464	.1735	-.0667	.7320	-.1904
Explained Variance	.8926	.8776	.7966	.7146	.4981	.1096
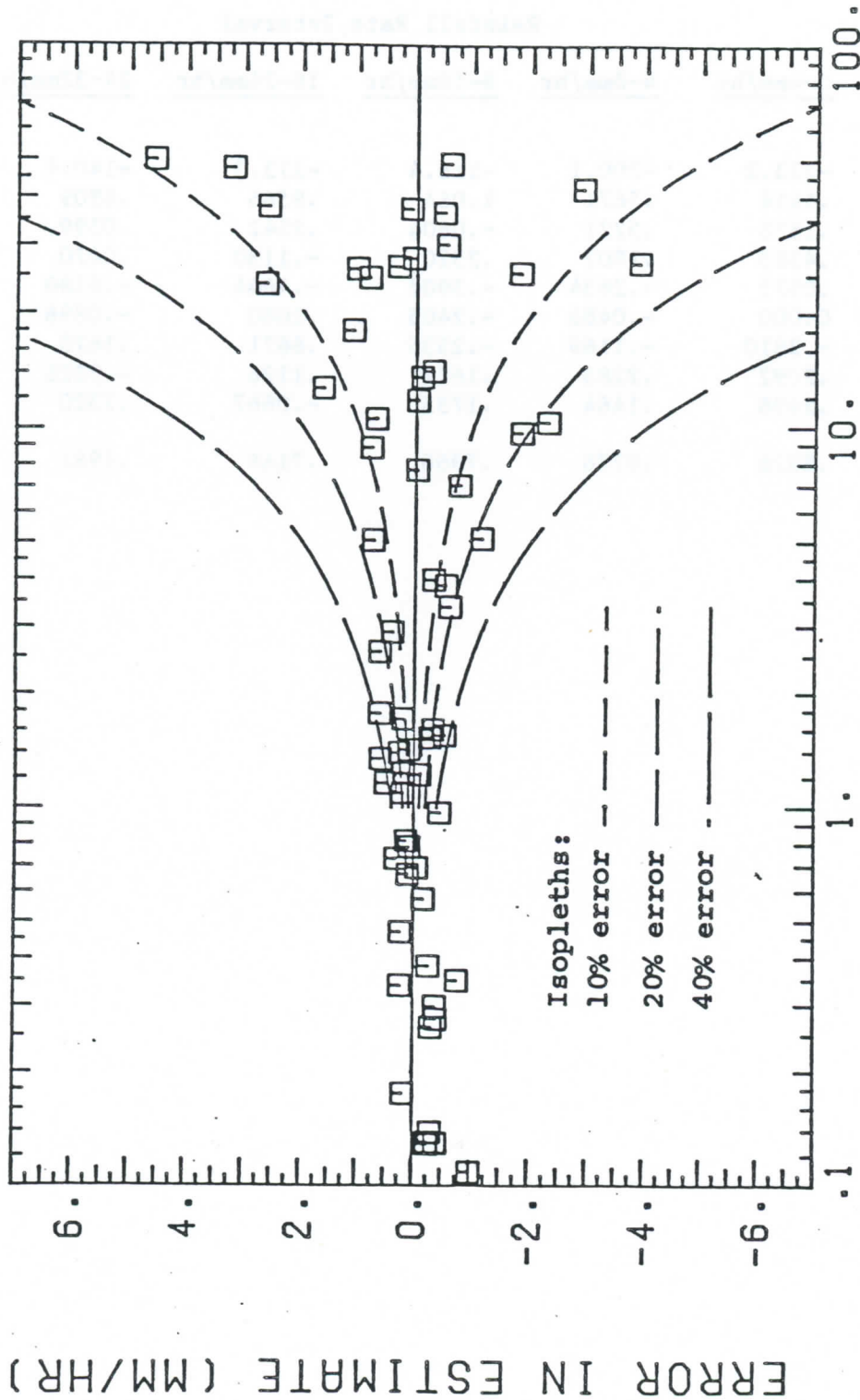
RAINFALL RATE (MM/HR)

Fig. 7.4 Errors in the inversion estimates of rainfall rate for $\sigma_{noise} = 2^{o}K$ in the regression/inversion data sets. The model atmosphere includes a .5 gm/m^3 LWC cloud droplet layer.

Restoration of Multichannel Microwave Imagery
To Estimate Rainfall Rates in Hurricanes

R. T. Chin, and C. L. Yeh,
Dept. of Elect. and Comp. Engr.
and
W. S. Olson and J. A. Weinman
Dept. of Meteorology

University of Wisconsin-Madison
Madison, Wisconsin   53706

Abstract

Eight synthetic multichannel microwave images, each having different spatial resolution, were restored to a common optimal resolution to estimate rainfall. The restoration utilizes a constrained iterative technique.

Restoration of Multichannel Microwave Imagery
To Estimate Rainfall Rates in Hurricanes

R. T. Chin, and C. L. Yeh   and   W. S. Olson, and J. A. Weinman
Dept. of Elect. and Comp. Engr.   Dept. of Meteorology

University of Wisconsin-Madison
Madison, Wisconsin   53706

I. Background

Multichannel microwave radiometers on the Seasat and Nimbus 7 satellites offer a quantitative method to measure rainfall amounts over the ocean. The emissivity of the ocean surface is low and varies predictably with wind speed; it thus provides a good background for observing precipitation. The theory and initial validation of this concept was given by Wilheit et al. [1]

Recently Olson [2] employed a radiative transfer model to simulate the polarized brightness temperatures that a Scanning Multichannel Microwave Radiometer (SMMR) would measure from hurricanes above sea surfaces at several frequencies. These brightness temperatures depend upon the rainfall rates, rain column heights, and the emissivities of the wind roughened sea surfaces. The information content of each channel is a variable function of these parameters and their relationships are nonlinear. A piecewise-linear regression algorithm was then applied to the synthetic data in the manner discussed by Smith and Woolf [3] to infer rainfall rates. The regression method employs data from eight of the SMMR channels.

Unfortunately, the size of the antenna of the SMMR on Nimbus-7 imposes a diffraction limit on the angular resolution such that the relative angular response, [H], of the radiometer is

$$[H(\theta)] = \left[\frac{2J_1(ka\ \sin\theta)}{ka\ \sin\theta} \right]^2 \tag{1}$$

where a is the antenna radius, θ is the angular deviation from the antenna centerline, $k = 2\pi/\lambda$ is the wave number and $J_1(\bullet)$ is the first-order Bessel function. The various channels of SMMR therefore each have a different footprint size (i.e., the 6.6, 10.7, 18.0, and 37.0 GHz channels with two polarizations have footprints of 148 x 95, 91 x 59, 55 x 41, and 27 x 18 km respectively). It is difficult to apply the regression algorithm unambiguously to real SMMR data because each channel measures radiation from an area which may contain differing amounts of rain. This study overcomes the diffraction limitation imposed on spatial resolution by means of image restoration.

II. Restoration of Spatial Resolution

The distribution of rain bearing clouds, $\vec{f}$, the observed microwave image, $\vec{g}$, the noise distribution, $\vec{\varepsilon}$, and the point spread function of the degradation, [H], are related by the following linear equation:

$$\vec{g} = [H]\vec{f} + \vec{\epsilon} \tag{2}$$

The inverse problem, in which $\vec{f}$ is derived from the measured $\vec{g}$ in the presence of noise, requires the inversion of Fredholm integral equations of the first kind. This linear inversion requires the existence and uniqueness of an inverse transformation $[H]^{-1}$. However, even if $[H]^{-1}$ exists and is unique, it may be ill-conditioned, so that a trival perturbation in $\vec{g}$ can produce nontrivial perturbation in $\vec{f}$. Thus, an ill-conditioned problem can produce undesirable effects such as noise amplification, resulting in grainy images.

This problem can be avoided by using a constrained iterative restoration algorithm to reconstruct the multichannel images. It is well established in the literature that a finite object has an analytic spectrum. Analyticity implies that knowledge of only part of the spectrum is sufficient to uniquely determine the remainder of the spectrum. Hence, the complete spectrum may be derived from the diffraction limited image of a finite object. This remarkable property has been applied with some success by Gerchberg [4], Papoulis [5], Papoulis and Chamzas [6], Howard [7], and Rushforth et al., [8] to invert one and two dimensional signals. This property also provides the theoretical basis for our method to match the footprints of multichannel microwave images.

The spatial image restoration can be considered as an operator, $\mathcal{O}$, chosen to estimate the portion of the spectrum of the actual rain field missed by diffraction limited imaging. The operataor $\mathcal{O}$ can be defined as the two-dimensional FFT of $\vec{g}$ within some known extent. The known extent of the hurricane is determined by the a priori information provided by the 37 GHz channel (the highest frequency channel of the SMMR with the best spatial resolution), and possibly visible and infrared images. The additional spectral components generated by $\mathcal{O}$ when added to the incomplete spectrum of the observed image, restores the resolution of the image. This process is then iterated to achieve optimal resolution.

III. Results

We initially utilized the 37 GHz channels to provide an a priori estimate of the spatial extent of the rain cells that is incorporated into the algorithm. Results of our initial investigation are shown in Fig. 1. A synthetic hurricane image was created in a 16 x 16 image field. Noise free antenna temperatures of both the 37 GHz and the 6.6 GHz channels were generated. The 37 GHz image regions that have no rain were used as a constraint to extend the resolution of the 6.6 GHz image data. Fig. 1a shows the cross sections of the rain cells in a synthetic image of a hurricane before and after the restoration. The degraded 6.6 GHz image resolution has been enhanced to a large degree after a few iterations. The synthetic images of the entire model hurricane that would be measured at 37 GHz, the original degraded 6.6 GHz, and the enhanced 6.6 GHz model hurricane rain cells are shown in Figs. 1b, 1c and 1d, respectively.

Data distorted by noise has rendered it difficult to continue the spectrum beyond the original diffraction limitation. Additional spatial and spectral constraints were therefore introduced to restore the noisy images.

The spectral constraints are based on a knowledge of the highest cutoff frequency (i.e., 37 GHz), and a knowledge of the degradation point spread function. More precisely, the magnitude and the phase information of a few low-

frequency components of [H] are derived and they are used to replace the magnitude and phase of the spectrum of the degraded image.

Spatial constraints are based on the estimated extent of rain areas, derived from 37 GHz, visible and infrared images, the upper and lower bounds of the measured brightness temperatures, and some physical attributes of hurricanes. Wind patterns around a hurricane are approximately axially symmetric with respect to the hurricane eye and we have incorporated this constraint as a preprocessing step to smooth out some of the noisy data. It has been demonstrated in our simulation that by performing a running average of the wind speeds along a circular sector around the hurricane, substantial noise is reduced.

The procedure to restore low frequency bandlimited images (i.e., the 6.6, 10.7, and 18.0 GHz) to the optimal resolution (i.e., the 37 GHz) is summarized in Fig. 2. This procedure has been applied to a set of noisy images. In one example additive white noise with an rms value of 4°K was added to both the 37 GHz and 6.6 GHz synthetic images. Within a few iterations, we obtained the restored image scan as shown in Fig. 3. The 6.6 GHz noisy image is nearly completely restored to the optimal resolution.

IV. Conclusions

The constrainted iterative restoration procedure has been demonstrated through computer simulations to be effective in restoring the spatial resolution of all of the SMMR channels to a 27 x 18 km footprint. An obvious next step is to apply this procedure to real SMMR data.

References

[1] Wilheit, T. T., A. T. C. Chang, M. S. V. Rao, E. B. Rodgers, J. S. Theon, "A Satellite Technique for Quantitatively Mapping Rainfall Rates over the Ocean," J. Appl. Meteo., 16, pp. 551-560, 1977.

[2] Olson, W. S., "Estimation of Rainfall Rates in Tropical Cyclones by Passive Microwave Radiometry," Ph.D. thesis, (in progress) Dept. of Meteorology, University of Wisconsin-Madison.

[3] Smith, W. L. and H. M. Woolf, "The Use of Eigenvectors of Statistical Convariance Matrices for Interpreting Satellite Sounding Radiometer Observations," J. Atms. Sci., 33, pp. 1127-1140, 1976.

[4] Gerchberg, R. W., "Super-Resolution through Error Energy Reduction," Optica Acta, 21, pp. 709-720, 1974.

[5] Papoulis, A., "A New Algorighm in Spectral Analysis and Bandlimited Extrapolation," IEEE Trans. Circuits and Systems, CAS-22,9, pp. 735-742, 1975.

[6] Papoulis, A. and C. Chamzas, "Detection of Hidden Periodicities by Adaptive Extrapolation," IEEE Trans. Acoustics, Speech, and Signal Processing, ASSP-27, 5, pp. 492-500, 1979.

[7] Howard, S. J., "Method for Continuing Fourier Spectra given by the Fast Fourier Transform," J. Opt. Soc., Am., 71, pp. 95-98, 1981.

[8] Rushforth, C. K., A. E. Crawford, and T. Zhou, "Least-Squares Reconstruction of Objects with Missing High-Frequency Components," J. Opt. Soc. Am., 72, pp. 204-211, 1982.
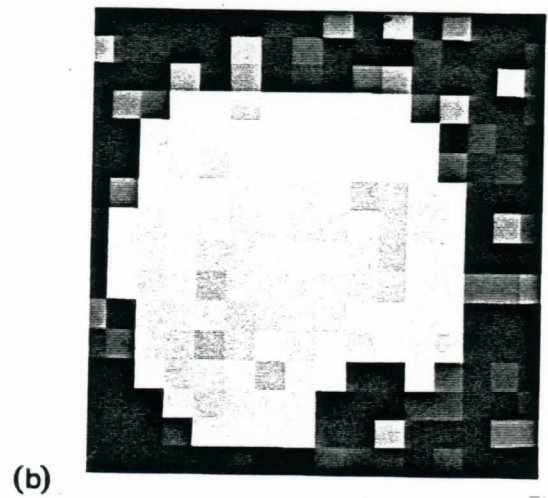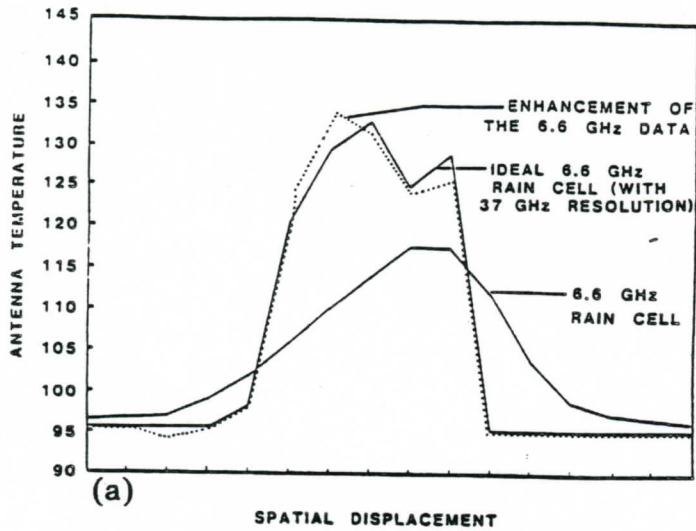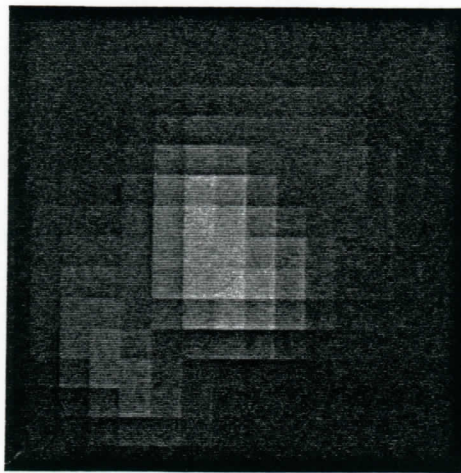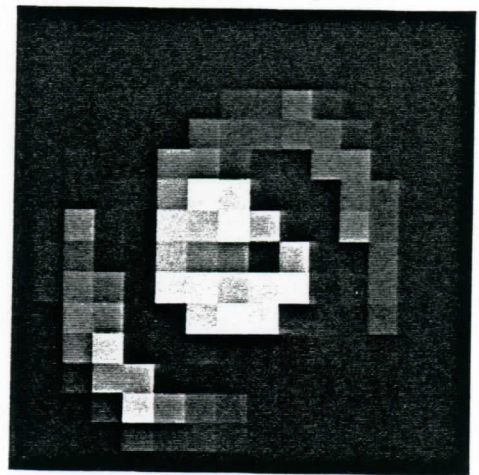
Figure 1: a) Enhancement of the resolution of a synthetic 6.6 GHz noise free image of a hurricane. This enhancement algorithm uses the known extent of the image shown in b) to enhance the degraded 6.6 GHz image shown in c). The derived enhanced image is shown in d).
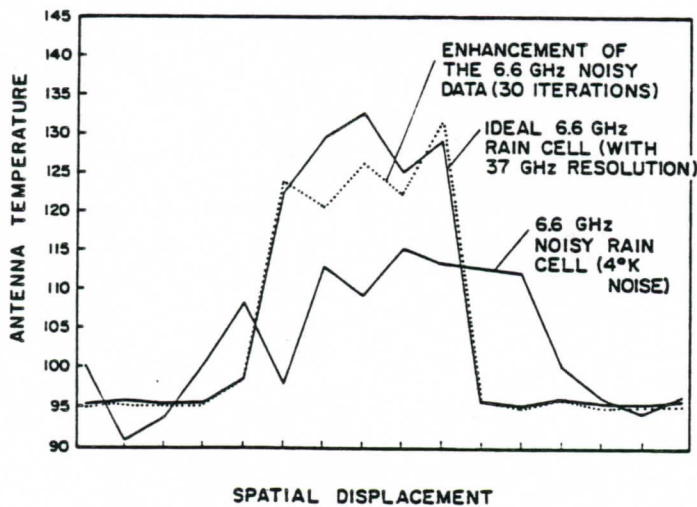

Figure 3: Restoration of Noisy Images.

Block Diagram of the Restoration Algorithm:
Figure 2